DEPARTAMENTO DE ASTROFISICA

Universidad de La Laguna

Master en Astrofísica

HIGH–*J* CO OBSERVATIONS WITH *HERSCHEL*–HIFI OF LOW– TO HIGH–MASS STAR–FORMING REGIONS

Irene San José García

LEIDEN OBSERVATORY
Universiteit Leiden

INSTITUTO Ð ASTROFISICA
Ð CANARIAS

La Laguna, Diciembre de 2010

SUPERVISORS:

Prof. Ewine van Dishoeck, Leiden Observatory, The Netherlands
Prof. Carlos Gutierrez de la Cruz, IAC, Spain
Dr. Lars Kristensen, Leiden Observatory, The Netherlands
PhD. Umut Yıldız, Leiden Observatory, The Netherlands

Index

1

Introduction

The main concepts related to star formation are presented in this Section. These include the current understanding of the evolutionary sequence both in terms of time and mass, as well as the chemical evolution in star-forming regions. This background is required for understanding the observations made with the *Herschel* Space Observatory[1] (Pilbratt et al. 2010) using the Heterodyne Instrument for the Far-Infrared, HIFI (de Graauw et al. 2010), presented in this report.

1.1   Young stellar objects

The origin of stars is one of the most fundamental questions in astrophysics, whose investigation has become active over the last forty years. This discipline has remained hidden a for long time because the star–forming regions are invisible optically, requiring advanced instruments and powerful telescopes at longer wavelengths to penetrate the dust. Nevertheless, over the last quarter of the twentieth century, important developments in the observational technology have opened the infrared and millimetre wavelength windows, being able to observe the dark clouds where stars born. These advances have represented a big step forward in our knowledge of the star formation process, laying down the ground for a theory of the origin and the early evolutionary stages of the stars.

Stars form in Giant Molecular Clouds (GMCs), which are very massive stable long–lived clouds, the dominant component of the interstellar medium (ISM) and a major constituent of the galactic disk. In those systems, any inhomogeneity tends to increase because of gravity; the denser regions show stronger gravitational pull on the surroundings and therefore they draw more material, becoming even denser. This gravitational collapse areas are places of active star formation, where the young stellar objects (YSOs) are created by contraction of those dense cores.

---

[1]Herschel is an ESA space observatory with science instruments provided by European–led Principal Investigator consortia and with important participation from NASA.

Once the molecular cloud collapses, a new protostellar object is formed, being deeply embedded in a thick envelope. In general, the opaque circumstellar gas and dust associated with the YSO extends to much further distances than the stellar atmosphere. Consequently, the emission from that dust will have a wide spectral distribution since it is in radiative equilibrium with the field of the forming star, which means the dust will exhibit a wide range of effective temperatures. As the protostar evolves, that envelope gradually dispersed due to two opposite mechanisms: a continued accretion onto the central star–disk system and a dissipation caused by the action of powerful outflows (another identified physical component of the YSO). However, the evolution of a protostar is closely related to its initial mass (amount of gas and dust from which it is formed) and to the specific chemistry of the original molecular cloud. Therefore, and in order to achieve a better understanding of the young stellar objects, a distinction across their masses will be done, with the aim of tracing the mass evolutionary sequence, highlighting the main characteristics of each type.
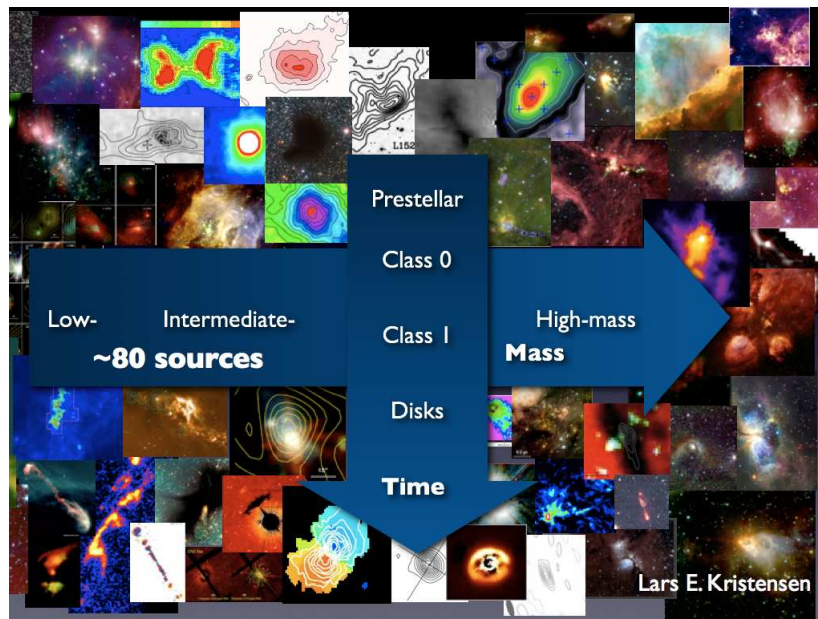
Figure 1.1: Mass and time evolutionary sequence of young stellar objects from L.E. Kristensen.

1.1.1 Low–mass sources

After the collapse of the cloud and the formation of the protostellar object, the envelope is heated by the accretion luminosity of the central source. The physical structure of the deeply low–mass (LM) embedded objects is complex, with a temperature and density gradient through its envelope and a marked disk at the center. In addition,

stellar jets are identified, which create cavities in the envelope affecting the surrounding material. For these objects it is possible to distinguish the different components of the YSO environment since they are located at less than 400 pc. Their characteristic bolometric luminosity does not achieve the 100 $L_\odot$ and their mass is are smaller than 5 $M_\odot$. However, the evolutionary status of a YSO cannot be derived knowing only its luminosity so its spectral energy distribution (SED) is required, particularly at infrared and sub–millimetre wavelengths. The shape and features observed in the spectrum depend on the nature and distribution of the surrounding material. The chosen scheme to classify these objects has been that proposed by Lada (1999), where four classes are categorized into two primary phases (Figure 1.2). This classification is used traditionally, but recent observations (e.g, van Kempen et al. 2008) have shown that this method is not very accurate determining ages. Nevertheless, and to follow the conventional path, Lada (1999) classification is presented:

- Protostars. They are the early embedded stage of evolution, when the star acquires mass through accretion of the surrounding material. The SEDs are dominated by emission from cold dust and peak in the sub–millimetre and far–infrared. Two classes are distinguished:

  Class 0: Embedded and extincted objects which cannot be observed using wavelengths shortward of 20 μm. Some of the main characteristics are their low temperature, 20-30 K, and their associated very highly collimated and energetic bipolar molecular outflows. They emit significantly more submillimeter radiation than other types of protostars. These class 0 objects are considered as the precursor of the class 1.

  Class 1: They produce significant infrared emission due to the dense molecular envelope and exhibit a silicate absorption feature at 10 μm. These objects also present bipolar molecular outflows but are less collimated and energetic than those observed in class 0 sources.

- Pre–main sequence stars: More advanced revealed stage, where most of the original surrounding material has already been incorporated into the young star. Its SED is characterized by a peak in the optical and near–infrared. Now the emission is dominated by the stellar photosphere.

  Class 2: For these objects, the SEDs are broader than a single blackbody function due to the radiation emitted by the luminous accretion disk surrounding the star. The disk spectrum is composed by a superposition of blackbodies of dust emission with different temperatures. There is still an infrared excess which indicates that there is circumstellar material associated with the source. T Tauri stars are examples of this kind of source.

  Class 3: These sources have a very little amount of circumstellar gas and dust and can be readily placed on the HR diagram. They are difficult to distinguish
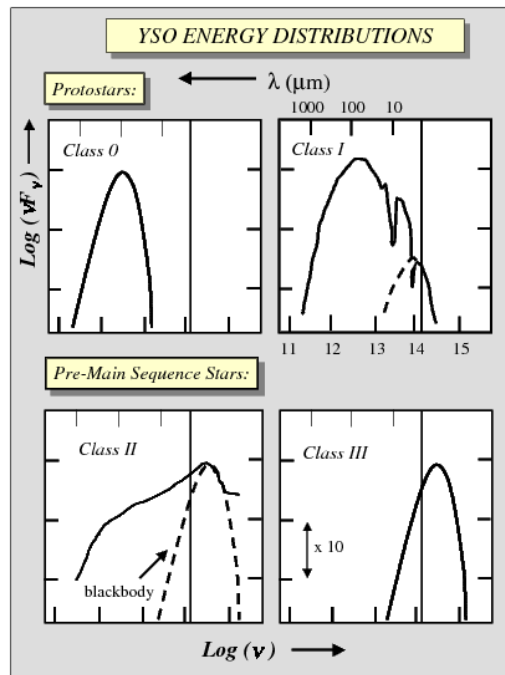
Figure 1.2: The empirical classification for YSOs spectral energy distributions, from Lada (1999).

from background stars in star formation regions. However, since they are relatively strong X-Ray sources, they can be identified in X–Ray surveys.

After presenting the different classes of low–mass YSOs, an evolutionary sequence can be found among their SEDs, corresponding to a gradual dissipation of gas and dust in the envelope due to accretion of the material by the star or due to its ejection. Therefore, the bipolar outflows become essential to achieve the formation and evolution of the protostar. Since the mass of the core where the star is born is more massive than the final formed stars, it suggests that, at some point, the source removes part of material by an active agent, the bipolar outflows.

1.1.2 Bipolar molecular outflows

The observation of high velocity outflowing CO gas changed drastically the idea of the gas kinematics in start forming regions. The agent which drives the bipolar molecular outflows prevails over the infall motions, an unexpected situation that explains the fact that not all cloud material is turned into stars. This suggests that during the evolution of the YSO, material from the surrounding cloud is removed by these bipolar outflows. These structures are present from the earliest stage of the protostars and are energetic enough to disrupt cold clouds. However, the driving agent of the bipolar outflows is still uncertain, with molecular jets, together with stellar

wind-component from the protostar the most feasible candidates.

Bipolar outflows are formed by the interaction of powerful winds emerging from the star with the surrounding molecular cloud. They extend over arcminute scales for nearby low–mass objects, exhibiting a large range in values of their velocity, degree of collimation, kinetic temperature, etc. This diversity could partially explain the evolutionary sequence of the protostar objects, and the role that these outflows play in it. One example was presented in the previous section, highlighting that an important difference between class 0 and 1 objects is related to the degree of collimation of their bipolar outflows.

Based on their shape and some other observable properties, two types of bipolar outflows are identified: the highly collimated and the classical outflows (Bachiller & Tafalla 1999). The large width of their emission lines indicate high–velocity molecular gas. The outflow material lies in two separated lobes of gas, one blue shifted and another red shifted, around the central emission.

- Classical outflow: The collimator factor, i.e, the ratio between the major and minor axes of the flow, $R_{\rm coll}$, is low in these cases (between 1 to 4), which means that the outflow is poorly collimated. An important aspect is the spatial distribution of the gas inside the lobes, finding shell geometries. The shell surrounds a cavity devoid of molecular gas (seen as a hole in ^{13}CO and a reflection nebula at optical wavelengths). This combination suggests that the outflow material represents ambient gas set into motion by an invisible wind from the central protostar. The driving agent is needed since the lobes and outflows can not be a direct ejection from the central YSO. These classical outflows are characteristic of the class 1 low–mass sources.

- Collimate outflow: The $R_{\rm coll}$ factor for these outflows is larger than 10, around an order of magnitude higher than for the classical outflows, achieving even 20 and 30 at high velocities. This means that the collimation increases with the velocity of the material set in motion. The high bipolarity of some molecular outflows rivals the strong collimation found in some optical jets, so jets and outflows could obey a cause–effect relation, being no longer two parallel phenomena with a different origin. Another difference with regard to the classical outflows is the existence of an additional component in the higher collimated ones. This component is a fraction of extremely high velocity (EHV) gas moving at much higher speeds (terminal velocities between 70 and 150 km s^{-1}). Those components can be easily identified in the spectra as discrete condensations called molecular "bullets" (they appear in one of the studied sources, L1448). The bullets show the violent and non steady state nature of the outflow phenomenon, injecting momentum into the ambient gas to produce lower velocity outflows. The collimated outflows are more energetic than the classical ones for sources of similar luminosity. The reason is not just because of the existence of the EHV

components, it is mainly because the central source is losing mass in a more violent way than the central sources of the classical outflows.

The indicated differences between both types of outflows can be understood in terms of outflow evolution. These structures decollimate as they evolve and their fraction of slow material with respect to the fast gas increases. These observational facts allow to propose an empirical evolution time sequence, where these structures pass from the highly collimated outflows with bullets (early class 0), passing through the less collimated ones without bullets (later class 0), to the classical outflows (class 1).

Nowadays, the possibility of getting deeper and exploring the cores of those objects is finally possible. Bipolar outflows represent an important perturbation in the chemistry of those cores, so they are an indispensable tool in the understanding of the evolution sequence for the YSOs.

1.1.3 Intermediate–mass sources

Intermediate–mas (IM) YSOs are considered the bridge between the low– and high–mass sources due to the values of their luminosity (10^2 to 10^4 $L_\odot$) and mass (5 to 10 $M_\odot$), among other physical and observational parameters. Since they are more massive than the low–mass sources, their timescales are shorter, becoming difficult to classify them in different evolutionary stages or classes.

The interest of these objects is not just because of the significant range of luminosity which they cover, but also because they are often found in clustered environments (so they can be used to investigate the more distant and confusing high–mass cluster regions). Therefore, the intermediate–mass sources are in an interesting regime where heating from the inside (from the central forming star) and also from the outside (radiation coming from the neighboring stars are important). This would mean a more extended warm zone, being able to create envelopes whose chemical structure is different from that observed in the low–mass YSOs. Therefore, there are many unresolved questions about these object related, for example, to the structures of their envelopes, the presence and characteristics of other components, their evolutionary sequence and the aspects that they share with and differ from other types of YSOs.

1.1.4 High–mass sources

The high–mass sources are characterized by masses and luminosities higher than 10 $M_\odot$ and 10^4 $L_\odot$, respectively. Even though the the number of these kind of objects is larger than the previous low– and intermediate– mass sources, their formation is not well understood and known, due to their large distances, their short timescales and the strong extinction suffered. Nevertheless, the embedded phase of the O and B stars formation can be divided into several classes, highlighting those four:

- Pre–stellar cores (PSC). They are the earliest stage, presenting the initial conditions. PSC are characterized with large column densities, low temperatures and the absence of outflow or maser.

- High–Mass Protostellar Objects (HMPOs). Considered the next evolutionary phase, the central star of these sources is surrounded by a massive envelope with a centrally peaked temperature and density distribution. They show outflows, whose existence is a sign of active star formation.

- Hot Molecular Cores (HMC). This next stage is characterized with large masses of warm and dense dust and gas, together with high abundances of complex organic molecules. These sources have big regions (more than 0.1 pc) with a high temperatures (more than 100 K).

- Ultracompact HII regions (UCHII). They are the final evolutionary stage of these YSOs. Large pockets of ionized gas have been developed, being still confined to the star. Once the parental molecular cloud is disrupted, a classical HII region is produced, signaling the end of the embedded phase.

Although a classification and an evolutionary sequence has been made for the high–mass YSOs along the above lines, they are not as well established as for the low–mass sources, because the physical and chemical processes which dominate each stage should be more studied and better characterized. Therefore, many key questions are still without answer: the consequences on the chemistry of the warm gas located close to the forming high–mass star, the kinematics of those cold and warm regions and characteristics of components like the outflows, in comparation with the structures studied in the previous types of YSOs.

This presentation of the different types of young stellar objects, together with their main characteristics, has established the background to perform a coherent and proper analysis of the data obtained with the HIFI instrument. The final aim will be not only achieving a deeper understanding of those objects, also finding a link from the low– to the high–mass sources, highlighting the main similarities and differences among them.

1.2   WISH key program

"Water In Star-forming regions with Herschel" (WISH) is a key program on the *Herschel* Space Observatory created to probe the physical and chemical structure of young stellar objects using water and other molecules as CO. Therefore, this key program follows the water abundances through the evolutionary sequence of those objects, from the collapsing clouds to planet–forming disks. WISH targets about 80 sources, covering a vast range of luminosities (from less than 1 $L_\odot$ to more than 10^5 $L_\odot$) and a wide range of evolutionary stages (from pre–stellar cores to warm

protostellar envelopes, passing through the observation of the outflows and finishing with the disks of the young stars). Two of the three instruments on *Herschel* are used to observe a big sample of H_2O lines, as well as its less–abundant isotopologues ($H_2^{17}O$ and $H_2^{18}O$) and chemically related species such as OH, H_2O^+ and H_3O^+. The Heterodyne Instrument for the Far Infrared (HIFI) makes single point observations of those lines at the source position, whereas the Photodetector Array Camera and Spectrometer (PACS) observes them in small maps around the protostar position, covering the outflows.

Water plays an important role in the protostar and planetary environments as one of the dominant form of oxygen, the third most abundant element in the universe, after hydrogen and helium. This molecule controls the chemistry of many other species, being a good tracer of the warm gas and the energetic processes present in the star formation regions. In addition, water is detected in cold areas in its solid phase (ice), facilitating the creation of planets. Some of the objects containing ice within protoplanetary disks, such as asteroids or comets, probably generated most of the water of our oceans, where life started. Finally, water also works as a coolant, contributing to the energy balance and to the collapse of clouds into higher temperatures. Therefore, the study of this molecule in these initial environments is crucial to understand not only the formation of protoplanetary systems, also the origin of life.

The WISH key program has already achieved some important results, which are witnessed through the publication of 15 letters in the *Herschel* and HIFI A&A special issues. Some of those establish the lack of water in cold gas at abundances lower than predicted, strong water emission from shocks in protostar systems, the importance of UV radiation in heating the gas along outflow walls and the unexpected widespread detection of the related hydrides OH^+ and H_2O^+ in outflows and foreground gas (Bruderer et al. 2010). More data and results are coming in the remaining two years of the lifetime of *Herschel* Space Observatory (already achieved the 65 % of the WISH observations).

In order to complement the water observations, high–frequency lines of CO, ^{13}CO and $C^{18}O$ are obtained. The CO J=10-9 line is one of the targets of this key program, together with the mentioned water lines, while the CO isotopologues are detected for free. These high–J lines are observed and spectrally resolved for the very first time in this key program, so many important results are expected. In addition, observation from ground based telescopes, as JCMT, IRAM 30m, APEX and other single–dish telescopes, are performed at lower frequencies aiming to obtain a global map of these young stellar objects. Therefore, the study of these additional lines and species is also indispensable in order to ensure a self–consistent data set for analysis.

1.3   CO observations

Due to its simple chemistry compared to other molecules (like water) and its high abundance, CO is one of the most important and used molecules to trace the different components of the protostellar systems. CO has a permanent dipolar moment (~ 0.1 Debye), so this molecule is easily excited and thermalized. For this reason, a measurement of the CO excitation provides an excellent estimate of the gas kinetic temperature. In addition, CO is an abundant molecule with strong lines, so it is detected along the protostar (in the envelope, outflows and disk). Specially, the molecular outflows are best traced by CO emission, being able to provide an outflow activity picture. Another property is related to its evaporation temperature, around 20 K for pure CO ice. This value is lower than that for H_2O, ~ 100, so the CO freeze–out zone is much smaller than the ones for water.

CO observations also include its isotopes, with various rotational transitions of ^{13}CO and $C^{18}O$ detectable at sub–millimetre wavelengths. $C^{18}O$ emission is associated with the protostellar condensations, while ^{13}CO line originates in the extended envelope and at the edges of the outflow. On the other hand, the emission from the ^{12}CO line wings refers to the material which is moving in the outflows. Therefore, those emission lines provide important and detailed information of the protostellar structure.

In addition, combining different rotational transitions for the same molecule or measuring the same rotational transitions for different isotopes, some physical quantities can be obtained. One example is the excitation temperature, T_{ex}, i.e, the temperature that characterizes the specific ratio of level populations. Another significant quantities is the optical depth, τ, which measures the transparency of a the line radiation, being able to obtain further parameters such as the gas column density of a species. These quantities are used to determine the distribution of a certain molecule through the protostellar system, acquiring a deep knowledge of the source (its geometrical, physical and chemical properties).

Knowing the importance of CO in the characterization of the YSOs, it is necessary to highlight the specific frequencies which should be used in order to identify the youngest sources, invisible until some decades ago. Since those are cold objects, the sub–millimetre range is the key interval to study and observe them. However, and aiming to look inside the dusty cold material surrounding the protostellar object, warmer regions are also observed, which means that part of far–infrared should be included in observation range. Therefore, knowing the wavelength interval of interest, and having the proper technology and telescopes, the aim of making these objects visible is getting closer everyday.

The main goal of this thesis is to find a possible link from low– to high–mass

sources, that is, discover the similarities and differences among these three types of young stellar object. For this reason, the main concepts and a global overview of YSOs and star–forming regions have been presented. Therefore, the background is established in order to make a detailed and accurate analysis of the available data, carrying out correlations and calculating of certain parameters.

2

Observations

Over the last decades, observation and radiative transfer modeling have provided considerable insight in the physical structure of protostellar envelope. Those observations were executed mainly from ground–based telescopes, like the JCMT, APEX, IRAM, etc. Thanks to the *Herschel* Space Observatory, operating at far–infrared wavelengths , further observations and analysis can be achieved, allowing a huge step in the knowledge of these objects. In this chapter, the telescope, instrument and technology used is described. This is followed by a description of the sources, lines and the reduction process applied to the data set. Hence, not only the improvements attained in observation techniques are presented, also those developed in the applied software.

2.1   Herschel and HIFI

The *Herschel* Space Observatory (Pilbratt et al. 2010) is an ESA cornerstone mission which carries the largest telescope mirror ever launched into space. This mission aims to explore the far–infrared and sub–millimetre wavelength range further than any previous space telescopes and with a higher angular and spectral resolution. Launched on May 14, 2009 and located in an L2 orbit, this observatory is equipped with advanced instruments and a primary mirror of a 3.5 m in diameter. *Herschel*'s science objectives are focused on examining the chemistry of the molecular Universe, studying dusty and relatively cool objects; particularly the birth of stars and their interaction with the interstellar medium, and the formation and evolution of galaxies in the early Universe. In order to achieve these goals, the observatory holds three instruments: a very high resolution spectrometer, the Heterodyne Instrument for the Far Infrared (HIFI) (de Graauw et al. 2010), an imaging photometer and integral field line spectrometer, the Photodetector Array Camera and Spectrometer (PACS) (Poglitsch et al. 2010) and an imaging photometer/Fourier transform spectrometer, the Spectral and Photometric Imaging Receiver (SPIRE) (Griffin et al. 2010). *Herschel* is expected to have at least 3.5 years of operation lifetime.

In this thesis, data from the heterodyne spectrometer, HIFI, were used and analyzed. This instrument is designed to provide very high spectral resolution, between 0.3 and 0.03 km s^{-1} (1.1 and 0.125 MHz), over a frequency range of approximately 480-1250 GHz and 1410-1910 GHz (625-240 and 213-157 microns). The diffraction limited at a frequency of 548.8 GHz is 42″, as given by formula $HPBW = 1.22 \cdot \lambda/D$. Therefore, the beam size decreases when the frequency increases, achieving 21″ at a frequency of 1101 GHz. Those values are smaller, by a factor of 3–5, than the beams of previous sub–millimetre space missions, such as SWAS or Odin.
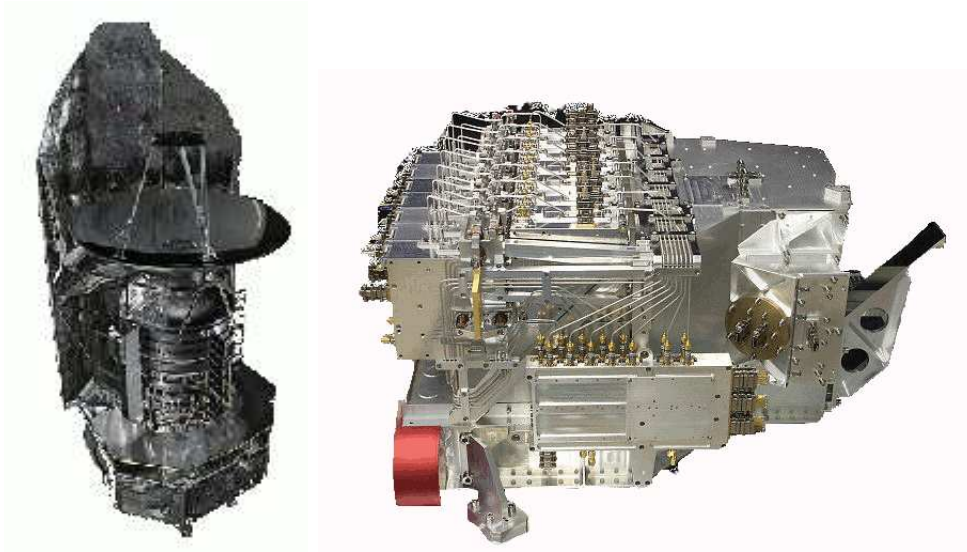

Figure 2.1: *Left.* The *Herschel* Space Observatory. *Right.* The high resolution spectrometer HIFI.

Line radiation at sub–millimetre wavelengths cannot use standard radio technology, since at these frequencies there are no good amplifiers available to amplify the weak sky signals. Combining the heterodyne technique with superconducting detector technology, HIFI is able to reach detection sensitivity close to the fundamental quantum noise limit and convert the sky signal to lower frequencies without losing the information carried on. This instrument works by mixing the incoming signal, $f_{\rm s}$, with another very stable and monochromatic signal, generated by a local oscillator, $f_{\rm LO}$. The result is a much lower frequency signal, $(\mid f_{\rm s} - f_{\rm LO} \mid)$, which is easier to amplify an radio wavelengths. Its frequency is called the intermediate frequency, IF, and it preserves the initial spectral information. Then, two different frequencies values of the source signal (lower and higher than $f_{\rm LO}$) can produce any of those specific IFs. Considering this for a range of incoming frequencies, two superimposed portions of an object's spectrum are measured by the spectrometer, resulting in the *dual sideband* (DSB) reception. The portion of the source spectrum above the $f_{\rm LO}$ is designated as upper sideband (USB) and that below $f_{\rm LO}$ as the lower sideband

Table 2.1: Overview of the spectral resolution and frequency coverage of the HIFI spectrometers HRS and WBS and the number of frequency bands.

Mode	HRS-High Resolution	HRS-Normal Resolution	HRS-Low Resolution	HRS-Wide Resolution	WBS Band
Number of bands	1	2	4	8	1
Bandwidth (MHz)	235	235	235	235	4000
Channel width (MHz)	0.125	0.25	0.5	1.0	1.1

(LSB). In some cases, when it is not known a priori which spectral lines are in which sideband or when the spectrum of the protostar is line–rich (for high mass sources for example), the f_{LO} is shifted 0.26 GHz for half of the integration time. This technique makes it possible to determine in which sideband the features of interest are and also to disentangle lines from the USB and LSB.

The mixing process is carried out in 7 receiver bands, that cover the aforementioned range. They can be divided into two groups depending on the mixer device used and the instantaneous frequency covered. Bands 1 to 5 use Semiconductor–Insulator–Semiconductor (SIS) mixer technology and the bandwidth of each band is 4 GHz. Bands 6 and 7 have Hot Electron Bolometer (HEB) mixers and they cover 2.4 GHz, having generally higher DSB noise temperature (factor of 8 between band 3 and 6).

HIFI has four backends, namely; a Wide Band Spectrometer (WBS) and a High Resolution Spectrometer (HRS) with two polarizations each, horizontal (H) and vertical (V). The WBS is an Acousto-Optical Spectrometer (AOS) which covers the full IF range available at a single resolution of 1.1 MHz. The HRS is an Auto-Correlator System (ACS) with several possible resolutions (from 0.125 to 1.00 MHz). However, its bandwidth at higher spectral resolution covers only portions of the available IF range, being able to split up and sampling more than one part. There are four different modes of operation for the HRS; wide band, low resolution, nominal resolution and high resolution mode, which involve distinct number of bands and reaches then different values of the resolution, see Table 2.1. The HIFI observations presented here have been taken in dual-beam switch mode with a nod of $3'$ using fast chopping.

2.2 Sources

2.2.1 Sample selection

The sources observed are spread over a wide range of luminosities and evolutionary stages, corresponding to the types of YSOs previously explained in the introduction. The sample is composed of 43 sources, of which 9 are low–mass class 0, 13 low–mass

Table 2.2: Overview of the main features of the lines of interest.

Mol.	Trans.	E_u/k_B	Frequency	HIFI	Beam	Exposure time on+off (s)			
		(K)	(GHz)	band	size ($''$)	LM 0	LM I	IM	HM
CO	10–9	304.2	1151.985	5a	20	598	412	598	–
^{13}CO	10–9	290.8	1101.349	4b	21	2431	1767	2431	438/2965
C^{18}O	5–4	79.0	548.831	1a	42	3599	–	1833	–
	9–8	237.0	987.560	4a	23	1217	1217	1025	418
	10–9	289.7	1097.162	4b	21	1767	–	1803	1727

class I, 6 intermediate–mass and the remaining 15 are high–mass sources. Summary information about them is presented in the Tables 2.3, 2.4, 2.5 and 2.6.

The criteria followed to choose these YSOs was based mainly on their luminosity, mass and distance. The low–mass targets have been selected from the list of the Andre et al. (2000), Jørgensen et al. (2009) and Evans et al. (2009), belonging to the Ophiuchus, Perseus, Serpens and Taurus molecular clouds. The luminosity of the sources are lower than 60 $L_\odot$ (stellar masses < 5 $M_\odot$) and they are situated no further than 450 pc. The intermediate–mass YSOs are characterized by luminosities from 10^2 to 10^4 $L_\odot$ (masses of a few to 10 $M_\odot$) and distances around 1 kpc. Surprisingly only two sources are found closer than 500 pc. These sources have been observed by other ground-based telescopes, e.g., Fuente et al. (2005) and Crimier et al. (2010). Finally, the set of high–mass YSOs is made up of 8 High–Mass Protostellar Objects, 4 Hot Molecular Cores and 3 Ultracompact HII regions. They are isolated sources located around a few kpc distance, being the furthest sources of the sample. Their luminosities and stellar masses are higher than 10^4 $L_\odot$ and 10 $M_\odot$, respectively. This sample of targets has been selected from several surveys by Molinari et al. (1996), van der Tak et al. (2000).

2.2.2 CO lines

The information of the observed CO and isotopologues lines is presented in Table 2.2. The isotopologues lines are obtained for free when specific water lines are targeted, so only the ^{12}CO (10–9) line is observed on purpose. Frequencies for different transitions and excitation energies were obtained from the *Leiden Atomic and Molecular Database* (`LAMDA`), and the beam size is calculated by the telescope diffraction limit formula, already introduced. Since the intensity of those lines depends on the mass of the source and its evolutionary stage, the exposure times chosen are different according to the kind of YSOs targeted. Usually, and for each CO line, the observing time of the low–mass and intermediate–mass sources is similar, however, it varies for the high–mass sources. The ^{13}CO (10–9) line is the best example, where some HM sources are observer for almost 7.3 minutes and others more than 48.3 minutes.

2.3   Reduction process

Most of the data used in this project are taken from the WBS for several reasons. First, these spectrometers cover the full IF range, so all the important line features occurring in this frequency range are sampled; second, the resulting spectral resolution is high enough for the frequencies of interest and finally the noise in the WBS data is lower than in the HRS data, by a factor of 1.4 when binned to the same spectral resolution. However, the velocity resolution achieved in the WBS for the $C^{18}O$ (5–4) line, $DV = 0.27$ km s^{-1}, was not sufficient to resolve properly the line profiles for the lowest–mass sources. For this reason, HRS data were used at this frequency for the low–mass object, attaining a resolution of $DV = 0.066$ km s^{-1}, (around 4 times higher than the WBS one). In the case of the intermediate–mass objects, it was impossible to work with the HRS data because there were no signal available for two of the sources.

The data reduction is easy to perform and follows some steps, which will be explained below and are summarized in Figure 2.2. The first step is executed by the HIFI pipeline in the *Herschel* Interactive Processing Environment (`HIPE`[1]) ver. 3.0.1 (Ott et al. 2010), where the obtained V_{LSR} precision is of the order of few m s^{-1}. Then, and thanks to the WISH live data show pipeline, developed by U. Yıldız and E. Deul, the spectra can be downloaded in a specific format which allows to deal with them in the `GILDAS-CLASS`[2] environment. This software is very flexible and makes it possible to carry out many accurate operations on the data and diverse representations of the spectra. Once the tools have been presented, the next steps of the reduction process will be explained in more detail.

Since two polarizations, horizontal and vertical, are observed simultaneously, these spectra are averaged together in order to improve the signal–to–noise. However, in some cases it is better to use only the H polarization data because the mixes have been optimized for this polarization. During this reduction process, if the discrepancy between the polarizations was smaller than 30%, the H and V spectra were averaged, (Figure 2.2.a). After that, the frequency and the velocity were modified to locate the line of interest at the correct velocity value, that is, on the velocity of the source with respect to the local standard of rest, V_{LSR}, (Figure 2.2.b). In order to complete the basic reduction, the intensity of the lines should be also modified and converted to the main–beam brightness temperature using the beam efficiency, η_{MB}, by the relationship: $T_{MB} = T_A^*/\eta_{MB}$. This coefficient indicates the fraction of power coming in the main Gaussian beam of the telescope, as compared to the total power. The value is the same for all the frequencies, however, it varies around the 5% among bands.

The next step is to subtract any possible baselines by fitting the spectra with low–

---

[1]HIPE is a joint development by the Herschel Science Ground Segment Consortium, consisting of ESA, the NASA Herschel Science Center, and the HIFI, PACS and SPIRE consortia.

[2]http://www.iram.fr/IRAMFR/GILDAS/

order polynomial functions, (Figure 2.2.c). In some cases this requires masking parts of the spectrum containing other lines to achieve a proper baseline subtraction. The reduction process is then finished, but other operations can be developed depending on the scientific aim. In order to obtain further information about the detected line, its profile was fitted with one or more Gaussian and its integrated intensity calculated, (Figure 2.2.d). Those are some of the many procedures available in this software package.
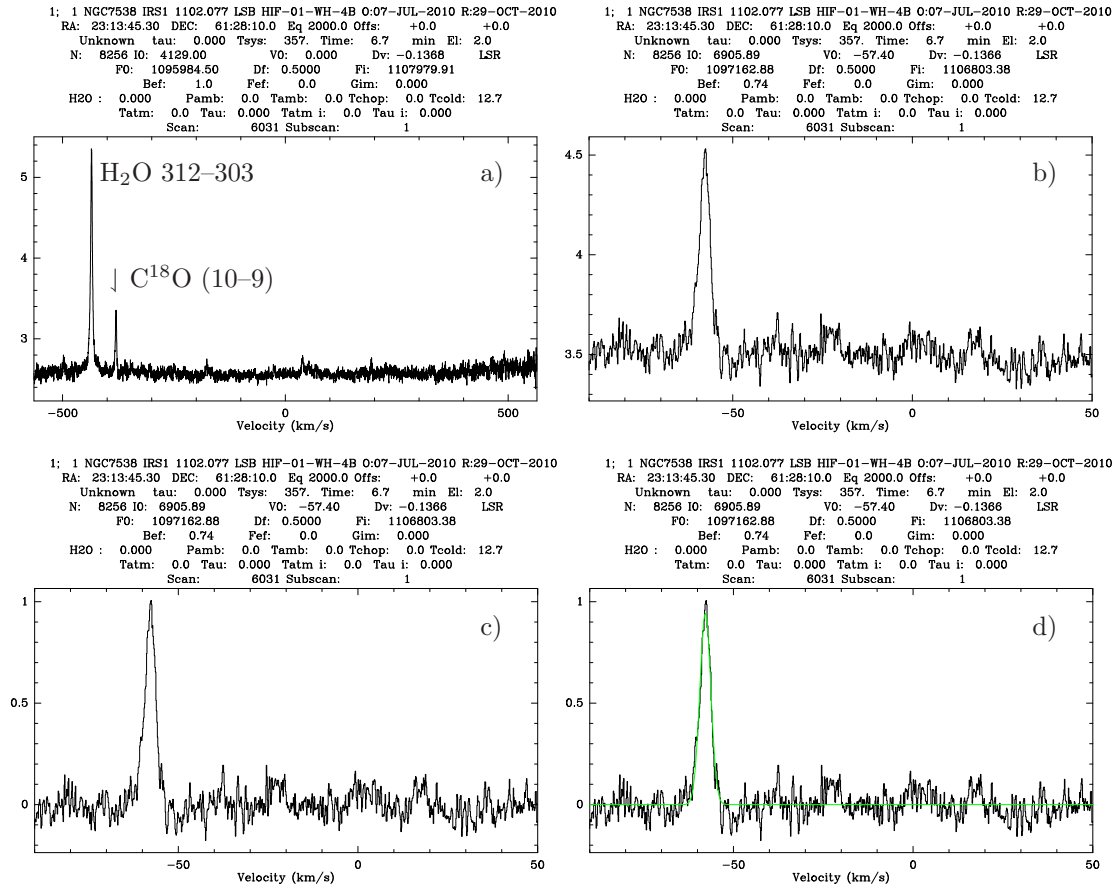
Figure 2.2: Reduction process summary of the high–mass source NGC7538–IRS1 for the $C^{18}O$ (10–9) line. *a)* Raw spectrum. In the header the initial values for the velocity, frequency and beam efficiency are seen, among others. *b)* $C^{18}O$ (10–9) line profile after modifying to the correct frequency. The line now appears at the right source velocity of -57 km s−1. *c)* Spectrum with the baseline subtracted, therefore the basic reduction process has finished. *d)* Line profile fitted by a Gaussian.

Table 2.3: Low-mass YSO Source List: Class 0

Source	Source Coordinates			Properties		
	RA (J2000.0)	Dec	$V_{\rm LSR}$	$L_{\rm bol}$	d	$M_{\rm env}$
	(h m s)	(° ′ ″)	$({\rm km\,s^{-1}})$	$(L_\odot)$	(pc)	$(M_\odot)$
L 1448-MM	03 25 38.9	+30 44 05.4	+5.3	11.6	250	1.5
NGC 1333 IRAS 2	03 28 55.6	+31 14 37.1	+7.7	20.7	250	1.0
NGC 1333 IRAS 4A	03 29 10.5	+31 13 30.9	+7.2	7.7	250	4.5
NGC 1333 IRAS 4B	03 29 12.0	+31 13 08.1	+7.4	7.7	250	2.9
L 1527	04 39 53.9	+26 03 09.8	+5.9	2	140	0.91
BHR 71	12 01 36.3	−65 08 53	−4.4	10	200	-
Ser SMM 1	18 29 49.6	+01 15 20.5	+8.5	30	250	-
Ser SMM 4	18 29 56.6	+01 13 15.1	+8.0	5.0	250	-
L 1157	20 39 06.3	+68 02 15.8	+2.6	6	325	1.6

Table 2.4: Low-mass YSO Source List: Class I

Source	Source Coordinates			Properties		
	RA (J2000.0)	Dec	$V_{\rm LSR}$	$L_{\rm bol}$	d	$M_{\rm env}$
	(h m s)	(° ′ ″)	$({\rm km\,s^{-1}})$	$(L_\odot)$	(pc)	$(M_\odot)$
L 1489	04 04 43.0	+26 18 57	+7.2	3.7	140	4.4
L 1551 IRS 5	04 31 34.1	+18 08 05	+7.2	28	140	1.7
TMR 1	04 39 13.7	+25 53 21	+6.3	3.7	140	0.12
TMC 1A	04 39 34.9	+25 41 45	+6.6	2.2	140	0.13
TMC 1	04 41 12.4	+25 46 36	+5.2	0.7	140	0.034
HH 46	08 25 43.9	−51 00 36	+5.2	12	450	-
IRAS 12496/HH54	12 53 17.2	−77 07 10.6	+2.3	50	200:	-
Elias 29	16 27 09.4	-24 37 19.6	+5.0	36	125	-
Oph IRS 63	16 31 35.6	-24 01 29.6	+2.8	1.6	125	-
GSS 30 IRS1	16 26 21.4	-24 23 04	+2.8	25	125	-
RNO 91	16 34 29.32	-15 47 01.4	+5.0		125	-
IRAS 15398/B228	15 43 01.3	-34 09 15	+5.1	1	130	-
Ced110 IRS4	11 06 47	-77 22 32.4	+3.5	1	125	-

Table 2.5: Intermediate Mass Source List

Source	Source Coordinates			Properties		
	RA (J2000.0)	Dec	V_{LSR}	L_{bol}	d	M_{env}
	(h m s)	($\circ$ $'$ $''$)	$(\mathrm{km\,s^{-1}})$	$(L_\odot)$	(pc)	$(M_\odot)$
NGC 7129 FIRS 2	21 43 01.7	+66 03 23.6	-10.0	430	1250	5
L1641 S3 MMS1	05 39 55.9	-07 30 28	5.0	70	500	-
NGC 2071	05 47 04.7	+00 21 44	10.0	520	450	-
Vela IRS 17	08 46 35.1	-43 54 31	4.5	670	700	-
Vela IRS 19	08 48 48.0	-45 32 29	12.2	776	700	-
AFGL 490	03 23 39.0	+58 36 35	-13.5	2000	1000	-

Table 2.6: High-mass YSO Source List

Source	Source Coordinates			Properties	
	RA (J2000.0)	Dec	V_{LSR}	L_{bol}	d
	(h m s)	($\circ$ $'$ $''$)	$(\mathrm{km\,s^{-1}})$	$(L_\odot)$	(kpc)
mIR-quiet HMPOs					
IRAS05358+3543	05 39 13.1	+35 45 50	-15.9	6.3×10^3	1.8
IRAS16272$-$4837	16 30 58.7	-48 43 55	-46.2	2.4×10^4	3.4
NGC6334-I(N)	17 20 53.3	-35 47 00	-4.0	1.7×10^4	1.7
W43-MM1	18 47 47.0	-01 54 28	$+98.8$	2.3×10^4	5.5
DR21(OH)	20 39 00.8	+42 22 48	-4.0	1.7×10^4	1.7
mIR-bright HMPOs					
W3-IRS5	02 25 40.6	+62 05 51	-38.4	1.7×10^5	2.2
W33A	18 14 39.1	-17 52 07	$+37.5$	1.0×10^4	4.0
AFGL2591	20 29 24.7	+40 11 19	-5.5	5.8×10^4	1.7
Hot Molecular Cores					
G327$-$0.6	15 53 08.8	-54 37 01	-45.0	1.0×10^5	3.0
NGC6334-I	17 20 55.2	-35 45 08	-6.7	1.1×10^5	1.7
G29.96$-$0.02	18 46 03.8	-02 39 22	$+98.7$	1.2×10^5	7.4
G31.41+0.31	18 47 34.3	-01 12 46	$+97.0$	1.8×10^5	7.9
UC HII Regions					
G34.26+0.15	18 53 18.6	+01 14 58	$+57.2$	2.8×10^5	3.3
W51N-e1	19 23 43.8	+14 30 26	$+57.3$	$1 - 10 \times 10^5$	5.5
NGC7538-IRS1	23 13 45.3	+61 28 10	-57.4	2.0×10^5	2.8

3

Results

In order to find a link between the different types of YSOs, the first step is to characterize the spectra, focusing on specific lines and extracting further information from their measured parameters. Therefore, in this chapter the reduced spectra of the observed sources are presented with the aim of highlighting their important characteristics and the features of the line profiles. This description will allow to develop a further analysis of the data and first conclusions.

3.1 Detected CO lines

The selected CO and isotopologue line profiles are presented in Figs. 3.1 to 3.13. This section will be divided in three parts, according to each type of YSO and in order to compare the results easily. Each subsection will detail the most representative aspects of the observed lines, aiming to find similarities and differences among them and among the sources. The characterization will be carried out, mainly by fitting the line profiles with one or two Gaussian functions. The parameters obtained from this fit (peak, width, position, area) provide essential information about the lines, such as the integrated intensity or the main beam temperature. Therefore, those values are calculated for any detected line and collected in Tables 3.2 to 3.6. Finally, a global overview will allow to clarify the principal differences between each type of YSO, providing useful information about them and about some significant and already studied spectral features.

3.1.1 Low–mass YSOs

The description will begin by focusing on the low–mass objects (Figs. 3.1, 3.2, 3.3, 3.4, 3.5 and 3.6). The given HIFI capabilities, the ^{12}CO (10–9) line is detected for all the observed YSOs, being the strongest and broadest among the other observed lines (Figure 3.1). The intensities of the lines are measured on main beam temperature scale. For this frequency and for those objects, the peak intensity ranges from 0.4 to 3.1 K, where the averaged value is 0.9 K. Another important parameter is the line

width, specified by the Full Width Half Maximum (FWHM). In this case, it varies from 2.4 $km\,s^{-1}$ to 21.3 $km\,s^{-1}$, and the average value is 11.5 $km\,s^{-1}$. Basically, for all the sources, different and unexpected structures are found in their spectra. This CO line profile can be decomposed into multiple components, a characteristic that has already been found in some water lines (Kristensen et al. 2010) and in ^{12}CO (10–9) (Yıldız et al. 2010). Also, in some of the profiles, a self–absorption feature at the source velocity is detected. Hence, this absorption cannot be caused by a foreground cloud, because those clouds have different velocities, which means that the absorption would appear some $km\,s^{-1}$ away from the V_{LSR}. This feature is seen in sources like BHR71, L1157 and TMC1. The symmetry of almost all lines is high, so no predominant blue or red shifted wing is seen. Finally, in L1448 spectra show other significant structures, the extremely high velocity (EHV) components of the outflows. They are located around 60 $km\,s^{-1}$ away from the source velocity and show how powerful these structures are and how fast the gas is moving.

In the Figure 3.2 the ^{13}CO (10–9) line profiles for the low–mass sources are represented. In this case, two of the three observed sources with low bolometric luminosity (L_{BOL}), L1157 and Ced110–IRS4, are not detected at this frequency down to 17 mK rms, indicating the need for longer exposure time for those faint objects. The intensity of these isotopologue lines is weaker than that of the ^{12}CO (10–9) lines by a factor of 6. So this fact, together with the lack of symmetry of their profiles, are the first differences between the spectra of these two molecules. The average intensity value is now 0.15 K and the range displayed goes from 0.08 to 0.45 K. Also, these emission lines are narrower than the ^{12}CO (10–9) lines, with NGC1333–IRAS4A as the source that shows the broadest profile with a FWHM of 12.9 $km\,s^{-1}$. The averaged value calculated for the lines width is 4.4 $km\,s^{-1}$. At this frequency, it is hard to identify multiple components or possible self–absorption features in the line profiles due to the noise. However, in NGC1333–IRAS4B and in L1489 are detected a weak absorption component at the source velocity, while NGC1333–IRAS4A present this kind of structure but shifted around 5 $km\,s^{-1}$ from the V_{LSR}. This means that can be caused by a foreground cloud with a different velocity.

The $C^{18}O$ (5–4) spectra are characterized by being less noisy and more symmetric than the ^{13}CO (10–9) spectra. The intensity of these lines ranges from 0.15 to 1.0 K, so they are also stronger than the lines observed at the ^{13}CO (10–9) frequency. However, they show, on average, smaller values of their FWHM, where the broadest width corresponds to Ser–SMM4 (4.54 $km\,s^{-1}$) and the narrowest width is found in L1157 (0.69 $km\,s^{-1}$). Those lines are well fitted with a Gaussian function, which means that no multiple components are identified. Nevertheless, in NGC1333–IRAS4B there is a weak absorption feature at the source velocity, being the only low–mass object which shows it at this transition. In Figure 3.3 the HRS and the WBS data are represented, in order to compare the resolution and the signal to noise, S/N, achieved by each spectrometer. The self–absorption structure in NGC1333–IRAS4B is not invisible

in the WBS data, being a good example of why the HRS data are needed at this frequency.

The $C^{18}O$ (9–8) lines are only detected in the sources with the highest bolometric luminosity, ($L_{BOL} > 20 \, L_\odot$), due to their weakness and noisy profiles, (Figs 3.4 and 3.5). These sources are; NGC1333–IRAS2 and Ser–SMM1 (class 0), Elias–29, GSS30–IRS1 and L1551–IRS5 (class I). However, only the objects with $L_{BOL} > 28 \, L_\odot$ have a clear line emission profile (see Tables 2.3 and 2.4). Due to the high noise, any component or structure in the line profiles is not detected, so no further information can be obtain from those spectra. The strongest intensity achieved is 0.14 K for Ser–SMM1 and the broadest line is observed in Elias–29 with a FWHM of 4.7 $km\,s^{-1}$. Finally, the $C^{18}O$ (10–9) line is also hard to detect owing to the noise and the existence of a strong water line (H_2O 3_{21}–3_{03}) really close to the frequency of interest (see Figure 3.6). NGC1333–IRAS2 is the only source that can be fitted with a Gaussian but the profile is still too weak. However, in the L1448–MM source it is quite difficult to disentangle the $C^{18}O$ (10–9) line from the spectrum, since the water line hides any relevant structure close by. Therefore, so far it is not possible to characterize the low–mass sources at this frequency.

3.1.2 Intermediate–mass YSOs

The total number of intermediate–mass sources observed at the frequencies of interest is six (Figs. 3.7 to 3.10). Therefore, in this subsection, a more detailed description of each YSO will be developed for each of the different CO and isotopologue lines. This characterization will allow to compare the results more deeply, with attention to other parameters that define the source, as its luminosity and distance. L1641–S3MMS1 is the IM source with the lowest luminosity. However, since it is also one of the closest objects, 500 pc away, a weak detection is found for the ^{12}CO (10–9), ^{13}CO (10–9) and $C^{18}O$ (5–4) lines. In the ^{12}CO line profile, two components can be identified, together with a weak absorption at the source velocity, V_{LSR}. The broad component appears red shifted from the V_{LSR}, which implies that the profile is asymmetric. The peak intensity is around 2 K, quite different compared with the values obtained for the low–mass YSOs. The ^{13}CO (10–9) line is very weak and noisy, being difficult to detect at this frequency. However, at the source velocity, a weak self–absorption feature is found, being significant within the noise. Similar to the low–mass sources, the $C^{18}O$ (5–4) line has the narrowest and most symmetric profile, so it is fitted with only one Gaussian. Finally, L1641–S3MMS1 is not detected at the $C^{18}O$ (9–8) frequency.

The nearest IM source is NGC 2071, with a distance of 450 pc. Due to its close location and high bolometric luminosity, four of the lines are detected, thus it is the strongest among this sample. The ^{12}CO (10–9) profile is also asymmetric and two components can be identified clearly, where width of the broader component is 21.6 $km\,s^{-1}$. Its mean beam temperature is almost 24 K, becoming the strongest
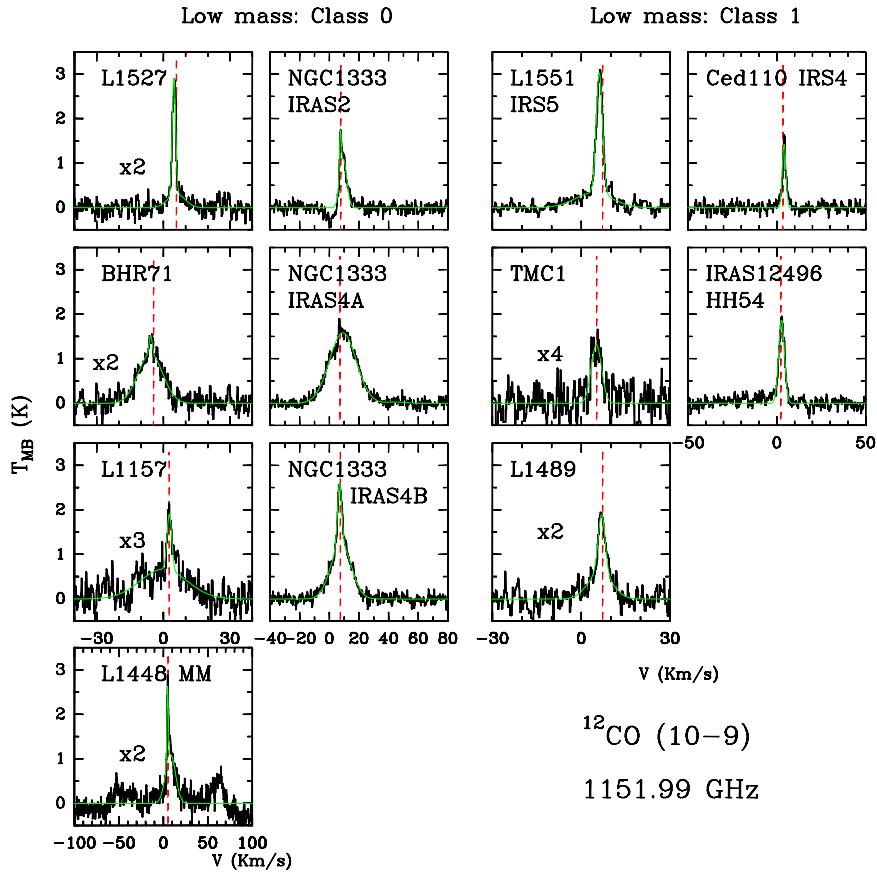
Figure 3.1: ^{12}CO (10–9) spectra of the low–mass YSOs observed. The channel size is 0.26 km s^{-1} and the V_{LSR} of each source is indicated by the red line. The different profiles have been fitted by one or two Gaussian.

line detected but among the low– and high–mass sample. The ^{13}CO (10–9) line is more symmetric than the ^{12}CO line, hence the existence of multiple components is not evident at this frequency. The intensity is 2.5 K and the FWHM is less than 4 km s^{-1}, quite different values compared with those obtained for the ^{12}CO line. At the C^{18}O (5–4) frequency, the line profile of this object is not as symmetric as for the other observed intermediate–mass sources. The reason is the existence of a small hump in the blue wing of its profile, which is presumably caused by a molecular outflow. No self–absorption or other structures are identified in this strong line. Finally, the C^{18}O (9–8) line is the weakest detected line for this source, with a peak intensity of 0.48 K and a FWHM of 9 km s^{-1}. The profile is not symmetric, being able to identify a broad and a narrower component. It is interesting to compare these results with those obtained for the L1641–S3MMS1 source, since they are situated at practically the same distance but they have different luminosity. NGC 2071, with 520 $L_{\odot}$, is more massive than L1641–S3MMS1, with 70 $L_{\odot}$, therefore, the differences observed between them could be related with this factor.

Vela 17 and Vela 19 are sources situated in the same molecular cloud and have
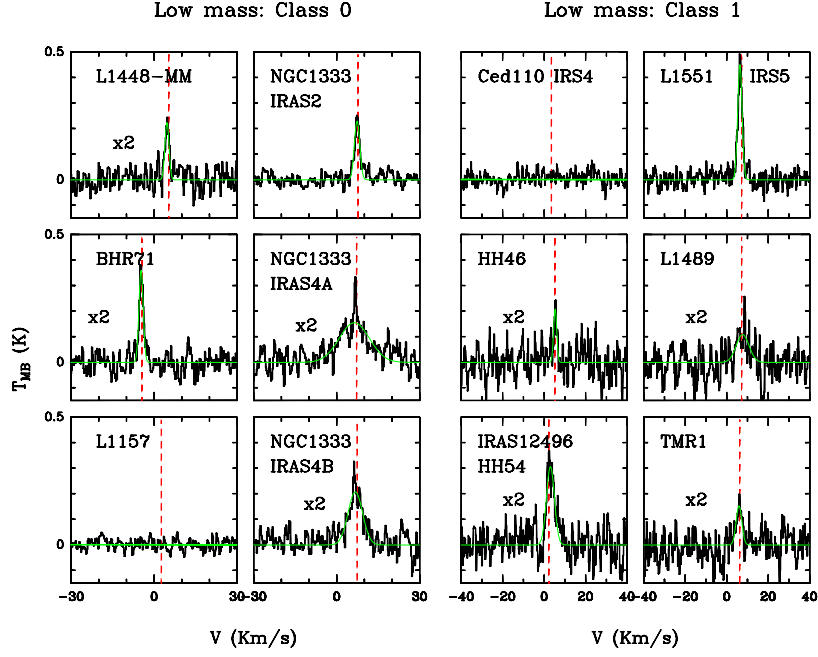
Figure 3.2: ^{13}CO (10–9) spectra of the low–mass YSOs observed. The channel size is 0.27 km s^{-1} and the velocity of the source is showed by the red line. The different line profiles have been fitted by one or two Gaussian.
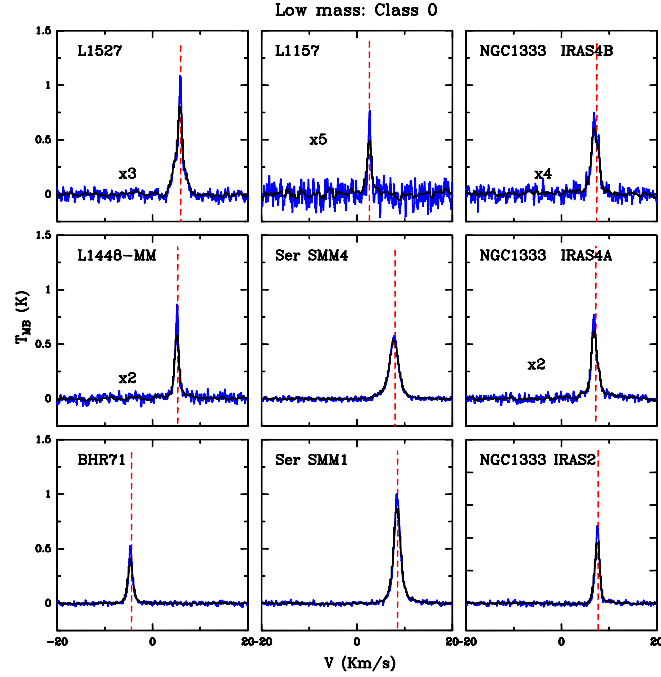

Figure 3.3: C^{18}O (5–4) spectra for the observed low–mass sources. The WBS data (black) are plotted on the top of HRS data (blue) in order to compare their resolutions.The channel size for the WBS data is 0.27 km s^{-1} and that for HRS is 6.6×10^{-2} km s^{-1}. The velocity of each YSO is specified by the red line.
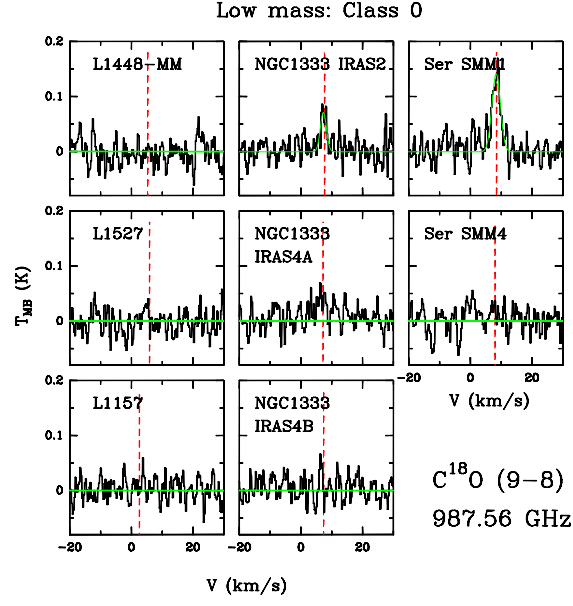
Low mass: Class 0

Figure 3.4: $C^{18}O$ (9–8) spectra for the low–mass class 0 YSOs. The size of the channel is 0.30 $\mathrm{km\,s^{-1}}$ and the velocity of each source is indicated by the red line. There are detections for only two sources, which have been fitted by a single Gaussian.
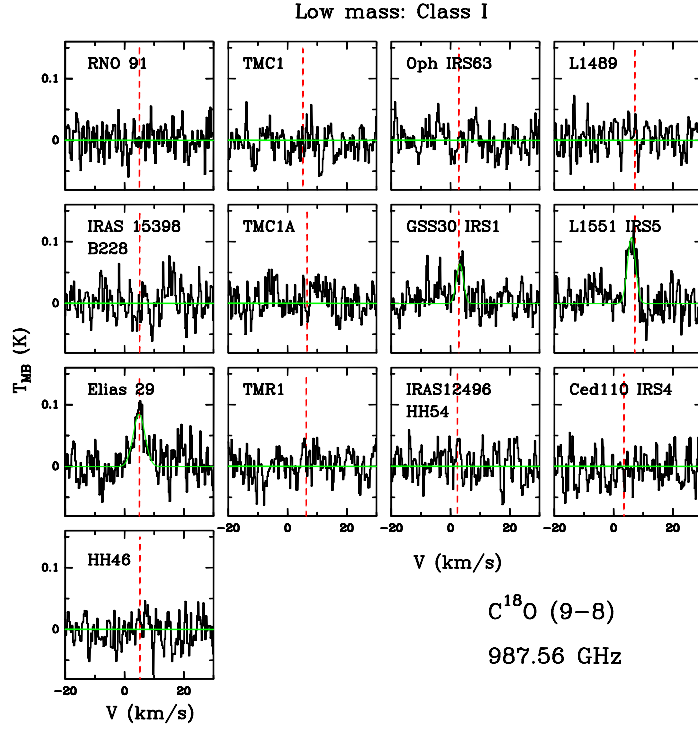
Low mass: Class I

Figure 3.5: $C^{18}O$ (9–8) spectra for the low–mass class 1 YSOs. The size of the channel is 0.30 $\mathrm{km\,s^{-1}}$ and the velocity of each source is indicated by the red line. Only three sources show a weak detection and their profiles can be fitted by a single Gaussian.
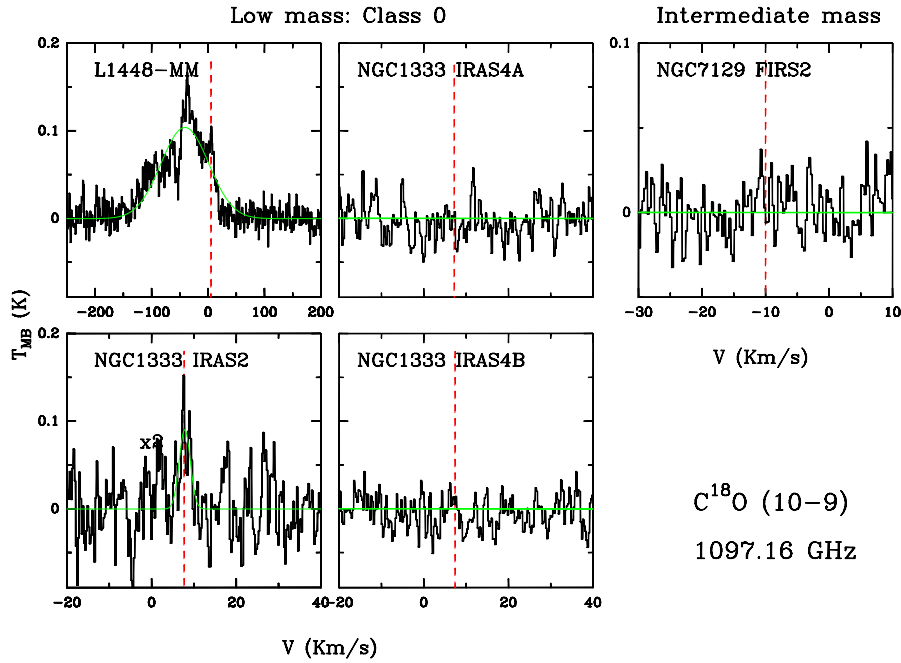
Figure 3.6: $C^{18}O$ (10–9) spectra for the low–mass and the intermediate–mass sources. The channel size is $0.27\ \mathrm{km\,s^{-1}}$ and the V_{LSR} is specified by the red line. One of the low–mass YSOs, NGC1333 IRAS2, shows a weak detection.

almost the same luminosity, 670 and 776 $L_{\odot}$ respectively. A similar behaviour is expected between them, however different features are seen in the observed emission lines. One example is the ^{12}CO (10–9) line: while Vela 17 shows a quite symmetric line profile (which fits perfectly with a single Gaussian), Vela 19 has a predominantly red wing, so multiple components are clearly identified on its profile. In the case of the ^{13}CO (10–9) line, the differences of their profiles are also significant. While Vela 19 shows a broader profile with a self–absorption feature, Vela 17 has a Gaussian like profile. As for the other IM sources, this line is noisier, being difficult to identify particular structures. On the other hand, the emission lines at the $C^{18}O$ (5–4) frequency are very similar and symmetric. Despite their symmetry, two components are found in both profiles, but the FWHM of the broader component is less than 9.5 $\mathrm{km\,s^{-1}}$. Nevertheless, one of the most interesting spectra belongs to the $C^{18}O$ (9–8) line. Since the profiles at the $C^{18}O$ (9–8) frequency are noisy, any structure cannot be easily defined and classified. It is important to highlight that, even though Vela 19 has a higher L_{BOL}, the intensity of its lines is always weaker than that measured in Vela 17. This could indicate that they are in different evolutionary stages, caused by the slight difference between their luminosities, which involves a difference in their mass.

The most distant intermediate–mass source is NGC7129–FIRS2, located at 1250 pc. Due to its distance, the observed lines are the weakest for this sample of objects. At the ^{12}CO (10–9) frequency, the emission profile is asymmetric and shows a FWHM
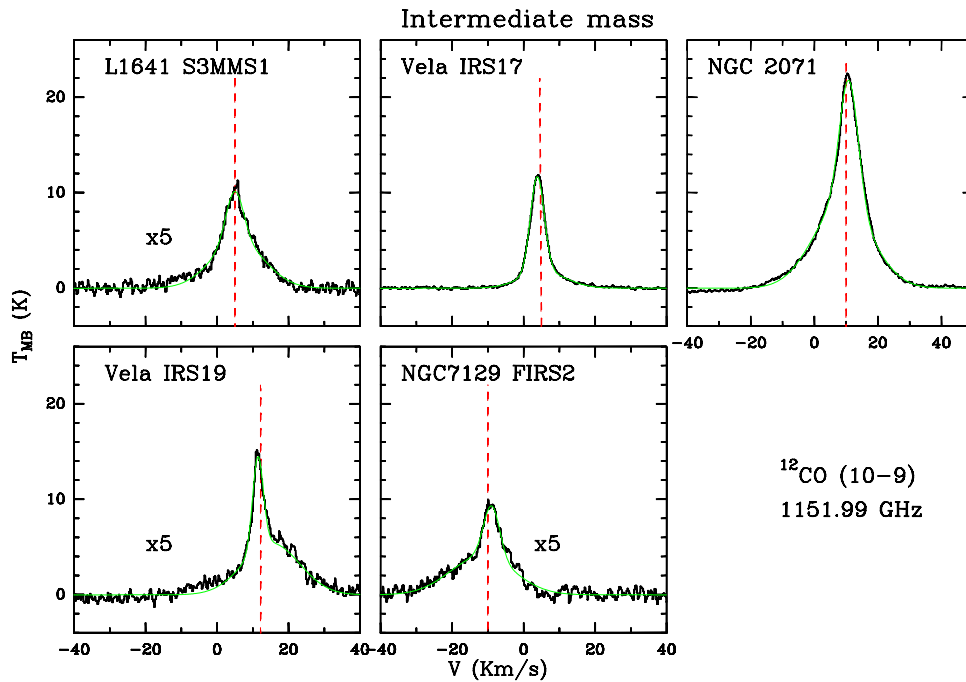
Intermediate mass

Figure 3.7: ^{12}CO (10–9) spectra for the intermediate–mass YSOs. The channel size is 0.26 km s^{-1} and the $V_{\rm LSR}$ of each source is indicated by the red line. The different profiles have been fitted by one or two Gaussian.

of 20 km s^{-1}. This component is quite wide, which means that the outflows are very energetic. In fact, this source has a powerful quadrupolar outflow, likely created by the superposition of two bipolar jets (Johnstone et al. 2010). No other significant structures are found. The ^{13}CO (10–9) line profile is noisier but can be easily fitted by a single Gaussian, so no multiple components are identified. In the case of the C^{18}O (5–4) line, its profile is quite symmetric but it can be properly fitted with two Gaussians. The FWHM of the broader component is only 7 km s^{-1}, almost insignificant if it is compared with the width of the broad component at the ^{12}CO (10–9) frequency. Therefore, the multiple component structure is not a characteristic feature. The C^{18}O (9–8) line is not clearly detected, probably because is located far.

In order to finish this subsection, the source AFGL490 is discussed, which has the highest bolometric luminosity (2000 $L_\odot$) but is also located very far (1 kpc, i.e, similar distance as NGC7129). The C^{18}O (9–8) line is the only line observed, therefore, no comparison can be made. Unlike NGC7129–FIRS2, for this source there is a weak detection at that frequency. Its study and observations will be interesting since its luminosity is completely different to that of the aforementioned source (430 $L_\odot$), which means also their masses and probably their evolutionary stage. The data of those objects can help to understand the evolutionary sequence of the YSOs at this range of luminosities, which can be used as "a small" scale link between low– and high–mass sources.
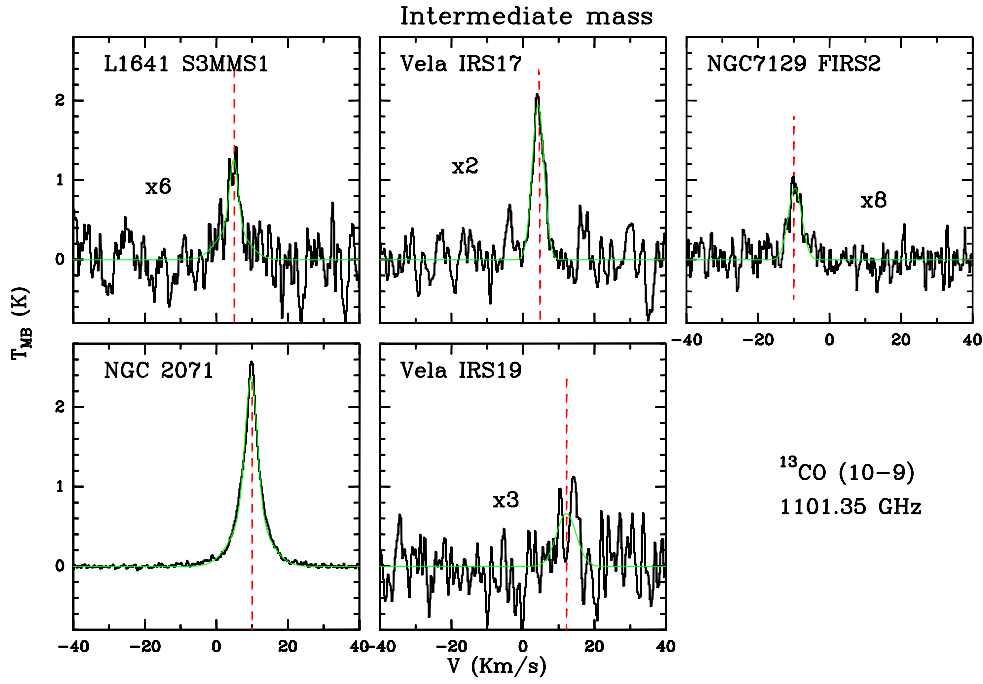
Figure 3.8: ^{13}CO (10–9) spectra of the intermediate–mass YSOs. The channel size is 0.27 km s^{-1} and the velocity of the source, V_{LSR}, is indicated by the red line. The different line profiles have been fitted by one or two Gaussians.
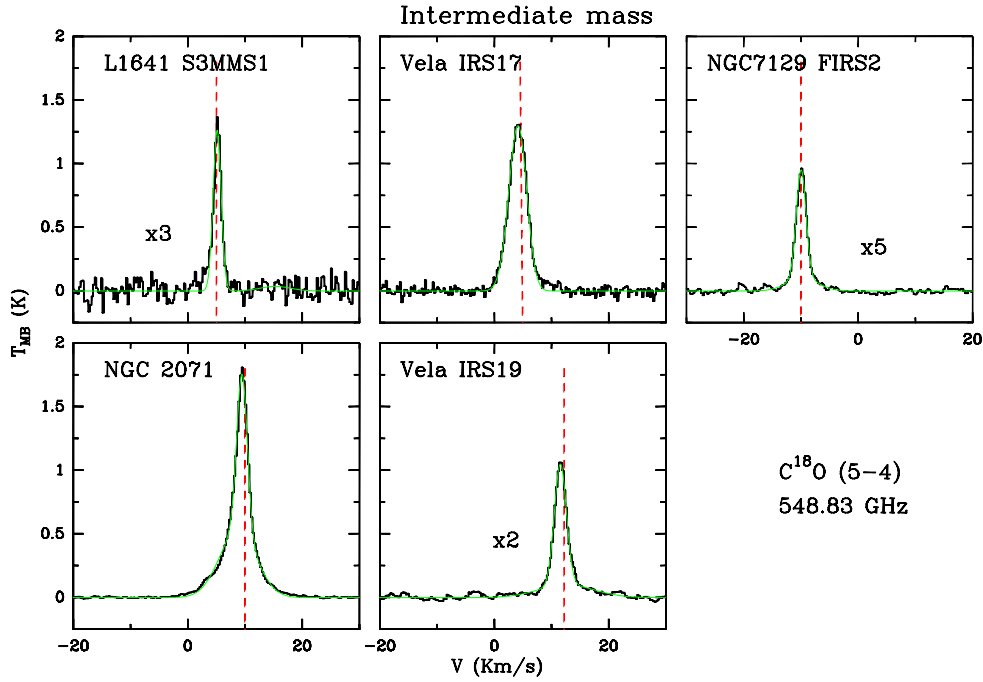

Figure 3.9: C^{18}O (5–4) spectra for the intermediate–mass YSOs observed. The WBS data are used, so the channel size is 0.27 km s^{-1}. The V_{LSR} of each source is specified by the red line and the lines profiles are fitted to one or two Gaussians.
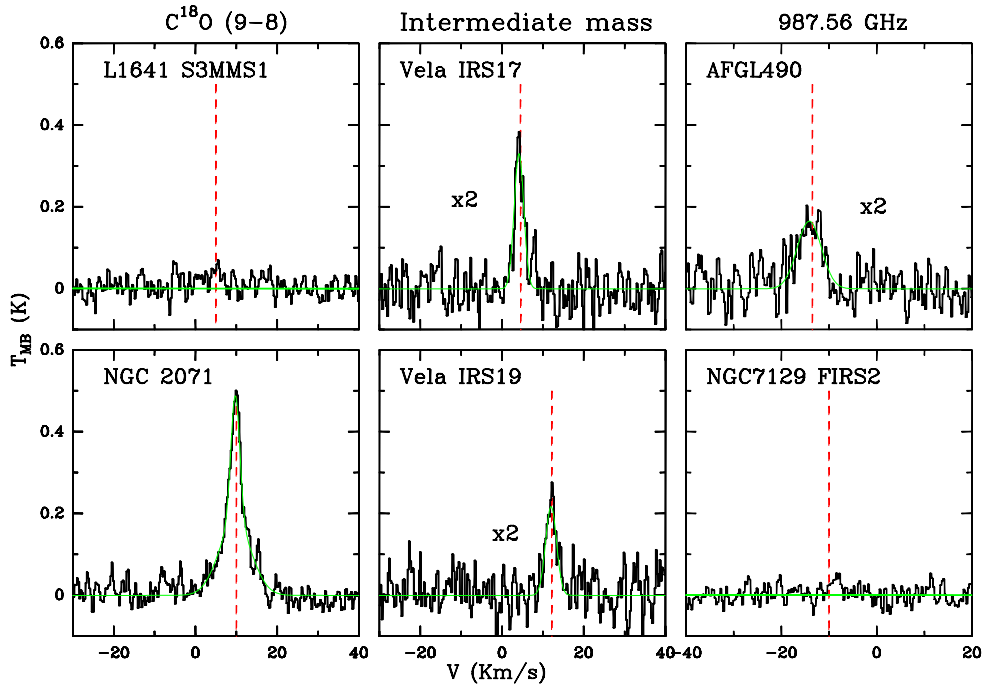
Figure 3.10: $C^{18}O$ (9–8) spectra for the intermediate–mass sources observed. The size of the channel is 0.30 $km\,s^{-1}$ and the V_{LSR} is indicated by the red line. The profiles have been fitted by a single Gaussian.

3.1.3 High–mass YSOs

The last part of this section concerns the high–mass YSOs, which have been targeted for only three of the CO isotopologue frequencies: ^{13}CO (10–9), $C^{18}O$ (9–8) and $C^{18}O$ (10–9). As for the low–mass sources, a general description of each line will be carried out, highlighting the more interesting features found in some sources. Global values will be provided in order to compare them with those obtained in the previously analyzed YSOs.

Therefore, this subsection will begin with the detected ^{13}CO (10–9) lines. Thirteen high–mass sources have been observed at this frequency, all of them showing quite strong and well defined line profiles. Even if different components can be identified, they are not as evident as the components found in the ^{12}CO (10–9) spectra of the LM and IM sources. Only W43–MM1 and G31.41+0.31 have been fitted by a single Gaussian profile. The reason is the presence of strong ripples and deep absorption structures nearby, which makes it impossible to perform a proper fit. However, in some high–mass sources, the existence of multiple components in their line profiles is quite evident, like for W3–IRS5, NGC7538–IRS1, NGC6334I–N, W51N–e1 and W33A. In order to compare and specify the value of the measured FWHM and peak intensities, their ranges will be presented. The averaged value for the width is 12.4 $km\,s^{-1}$, and the FWHM values range from 6 to 20 $km\,s^{-1}$. Those broader components are red or blue shifted, depending on the source, breaking the symmetry of

their profiles. Comparing the profiles with those obtained for the LM and IM sources at this frequency, an important fact is seen: the rms is significantly lower so the lines are well defined. This also allows to identify other structures, such the absorption features seen in the W51–e1 spectrum. One is locates at the source velocity, so can be caused by the cold cloud surrounding the envelope. The other one is located around 6 km s^{-1} away from the V_{LSR}, hence it is probably created by a foreground cloud. In terms of intensity, the average value is 3.2 K, stronger than that achieved by the other types of YSOs at this frequency. For W3–IRS5, which is the closer source (2.2 kpc) with the higher luminosity (1.7×10^5 $L_{\odot}$), the peak main beam temperature reaches almost 20 K.

The profiles obtained for the C^{18}O (9–8) lines are less strong and all of them have been fitted by a single Gaussian profile, since no clear multiple components are identified. Nevertheless, structures like self–absorption are more evident and important. Those are found at the source velocity in DR21–OH, G327–0.6, W51N–e1, W33A and W43–MM1, but due to the noise, they are difficult to identify. The average width is 5.2 km s^{-1}, similar to the value obtained for the IM objects (5.3 km s^{-1}), and the values range from 3.3 to 6.8 km s^{-1}. These profiles are symmetric however, few of them, like G327–0.6, show strong structures close to the emission line of interest. The averaged main beam temperature is 1.4 K, still the highest detected at this frequency.

Finally the C^{18}O (10–9) lines will be examined. They are similar to the C^{18}O (9–8) lines, in terms of the intensity and width of their profiles. The average value of those parameters are 1.0 K and 4.8 km s^{-1}, respectively, and the FWHM ranges from 3.3 to 6.4 km s^{-1}. The lines are symmetric but a strong water line (H$_2$O 3_{21}–3_{03}) is nearby in frequency, so the profiles are quite affected by it. Therefore, additional operations have to be made in order to fit the lines properly. This fact, together with the increase in the noise, prevent to extract further information about these spectra. The best examples are W43–MM1, W33A and IRAS05358+3543 in terms of noise and W3–IRS5, NGC6334I–N and NGC6334–I in terms of ripples near to the line of interest. No self–absorption features are identified in any of the emission profiles. Since at this frequency, the detections are weak or even nonexistent for most of the low–mass and intermediate–mass sources, no further comparison can be made. It is interesting to note that the C^{18}O (10–9) line is only visible in protostellar clouds with high luminosities, so it could be already a result or at least a sign that longer exposure times are needed for the other types of YSOs.

3.2   Multiple components

In the detailed description carried out in the last section, the existence of multiple components has been highlighted as one of the more significant and important features found in some CO and isotopologues line profiles. Those kind of structures have been already identified in water line profiles for low–mass (Kristensen et al. 2010)
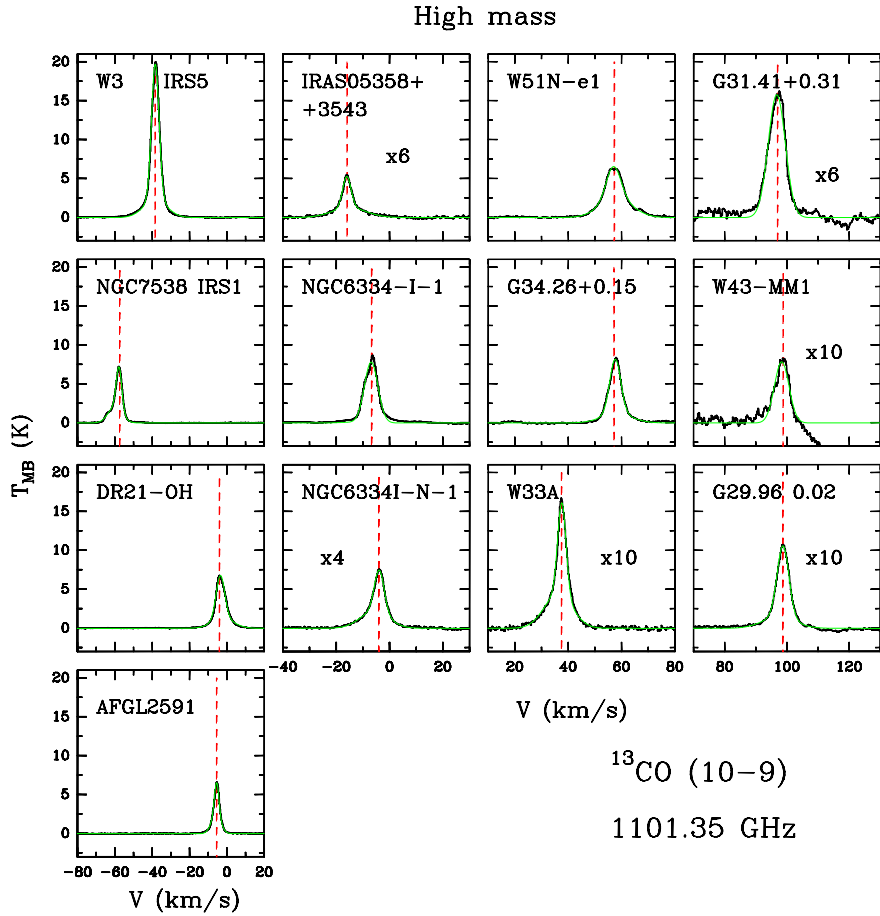
High mass

Figure 3.11: ^{13}CO (10–9) spectra of the high–mass YSOs observed. The channel size is 0.27 km s^{-1} and the V_{LSR} is indicated by the red line. The different line profiles have been fitted by one or two Gaussian.

and in CO lines (Yıldız et al. 2010), intermediate–mass (Johnstone et al. 2010), and high–mass protostars (Chavarría et al. 2010). Kristensen et al. (2010) propose a classification and an explanation of the three components that have been identified in some observed water lines. All of them are centered close to the source velocity and their characteristic parameters are obtained by Gaussian fits. The different components can be divided in broad emission components, with a FWHM > 20 km s^{-1} and sometimes offset from the source velocity; medium–broad emission structures, where the FWHM can vary from 5 to 10 km s^{-1}; and narrow emission or self–absorption components, with a FWHM of about 2 km s^{-1} and located at the source velocity, V_{LSR}. The proposed explanation is that the broad components are caused by shocked gas along the outflow cavity walls, the medium are most likely caused by smaller spatial scale shocks, created by the outflow in the inner (< 1000 AU) dense envelope, and the narrow absorption components come from the quiescent cold envelope.

These structures have been identified in some of the studied line profiles in this
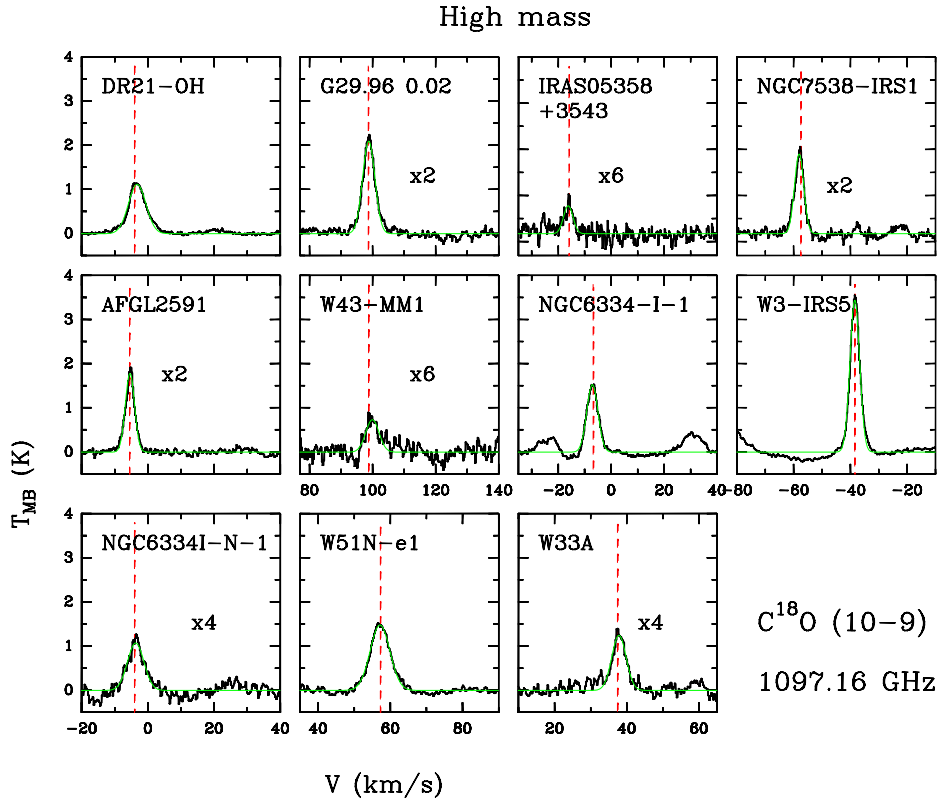
High mass

Figure 3.12: $C^{18}O$ (10–9) spectra for the high–mass YSOs observed. The channel size is 0.27 km s^{-1} and each source velocity is specified by the red line. The profiles have been fitted by a single Gaussian.

thesis, but are less prominent than those seen in the water lines. The narrow self–absorption component is significantly weak, being hard to distinguish from the background noise. The ^{12}CO (10–9) lines are those that show most clearly the multiple components profile, especially the spectra from the intermediate–mass sources. In order to perform a proper analysis of these structures, the widths and integrated intensities of the two components, in which their profiles can be divided, have been calculated. The results are presented in the Table 3.1. However, the values obtained differ in some aspects from those defined by the water–line observations. In the case of CO, the medium–broad components are always narrower than 6 km s^{-1}, differing from the range determined by Kristensen et al. (2010). Also, some of the broad components do not reach the 20 km s^{-1} FWHM lower limit, mainly the line profiles originating from the LM sources.

These results show that the multiple components found for the CO lines are generally between 3-8 km s^{-1} smaller than the components detected in the H_2O lines. The best examples are plotted in Figures 3.14 and 3.15. They are two different types of YSOs, whose components have been identified and fitted by two Gaussians. According to the proposed classification, the FWHM of the broader component for the class
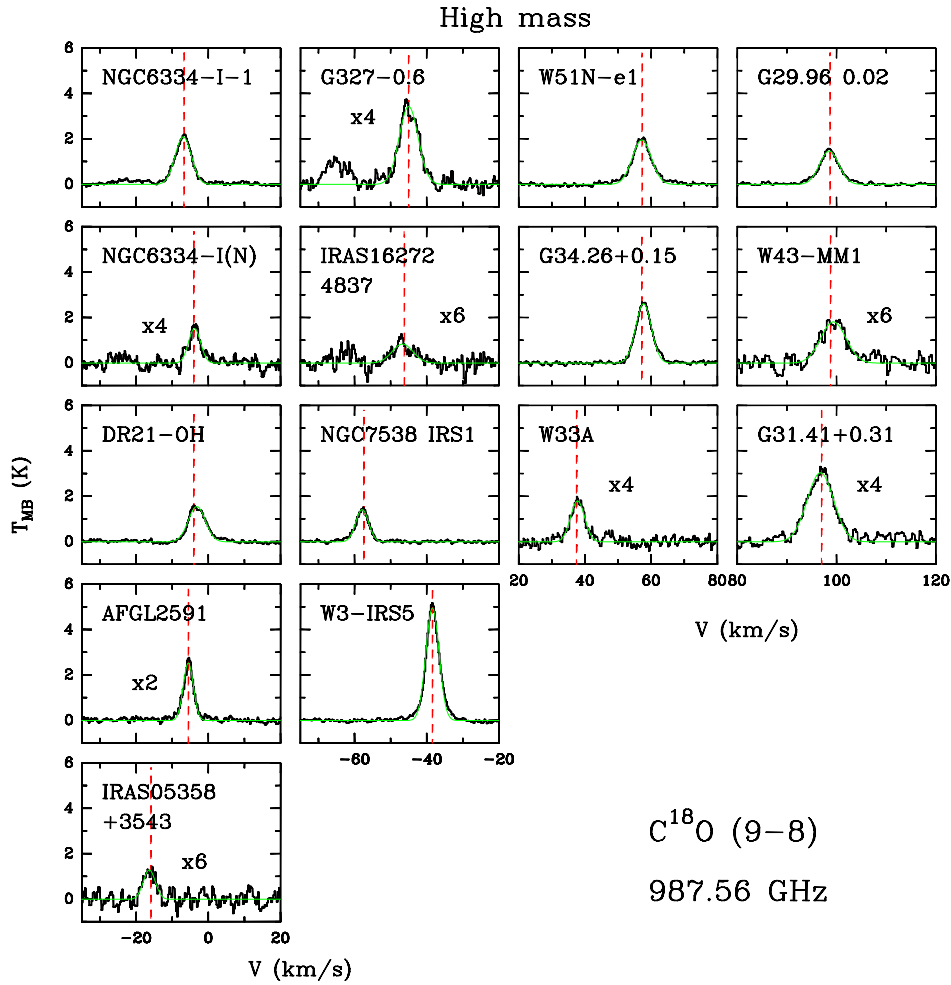
High mass

Figure 3.13: C^{18}O (9–8) spectra for the high–mass sources. The size of the channel is 0.30 km s^{-1} and the V_{LSR} is indicated by the red line. The profiles have been fitted by one Gaussian.

0 source L1488–MM, Fig. 3.14, is only 13 km s^{-1}, more similar to a medium–broad structure than to a broad one. The same behaviour is observed for the narrower emission component since its FWHM value is 1.7 km s^{-1}, instead of between 5 to 10 km s^{-1}. The self–absorption feature is not detected, so more differences are added with respect to the water line profiles. On the other hand, the IM source Vela 19 has a broad component, 20.6 km s^{-1}, similar to those identified in the H$_2$O lines. However, the "medium–broad" emission component has a FWHM of 3.2 km s^{-1}, being also smaller than the proposed values in Kristensen et al. (2010). A weak self–absorption structure is seen, but it is too weak to be studied properly.

In this chapter, the results obtained from the description of the morphological features of the CO and isotopologue lines have been presented. The next main purpose is to perform a proper analysis of these highlighted structures, in order to understand what they mean and which mechanism caused them. Therefore, different correla-

Table 3.1: Integrated intensity and width of identified multiple components in the ^{12}CO (10–9) spectra.

Source	Broad		Medium	
	$\int T_{MB}dV$	FHWM	$\int T_{MB}dV$	FHWM
	(K km s^{-1})	(km s^{-1})	(K km s^{-1})	(km s^{-1})
Class 0				
L 1448-MM	7.0	12.9	1.5	1.6
NGC 1333 IRAS 2	4.7	5.5	3.0	1.5
NGC 1333 IRAS 4A	33.9	21.3	3.0	2.1
NGC 1333 IRAS 4B	20.6	16.2	4.8	3.3
L 1527	1.6	9.3	2.5	1.8
BHR 71	7.6	24.8	0.3	2.5
L 1157	6.5	13.3	1.3	1.8
Class I				
L 1489	1.9	9.4	2.0	2.2
L 1551 IRS 5	5.9	14.9	7.1	2.5
TMC 1	3.2	4.1	2.3	1.4
IRAS 12496/HH54	1.8	3.9	6.5	1.5
Ced110 IRS4	1.9	2.4	2.1	1.2
Intermediate mass				
NGC 7129 FIRS 2	18.2	20.9	6.3	5.3
L1641 S3 MMS1	17.9	17.6	7.6	5.7
NGC 2071	216.0	21.6	116.5	7.0
Vela IRS 17	27.9	15.2	48.9	4.6
Vela IRS 19	26.6	18.4	6.6	3.5

tions are needed in order to find relationships among the different parameters. Those parameters characterize each source, so more information about them will help to discover a link among the different types of YSOs.
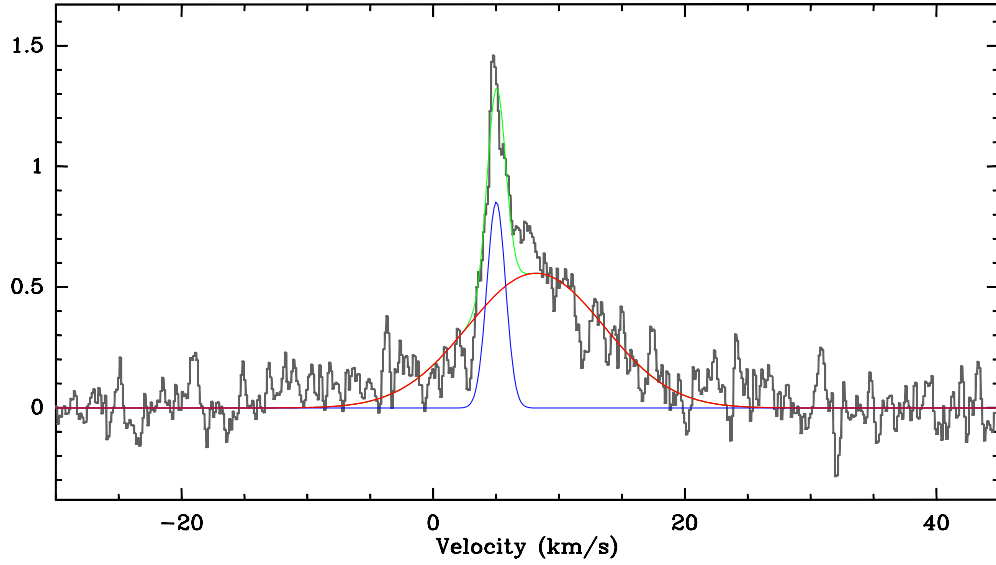
Figure 3.14: Spectrum of the ^{12}CO (10–9) transition (grey) of the low–mass class 0 source L1448–MM, and superposed with a Gaussian fit (green). The fit includes a narrow component, 1.7 km s^{-1} FWHM, centered at 5.0 km s^{-1} (blue), and a broader component, 12.7 km s^{-1} FWHM, redshifted at 8.2 km s^{-1} (red).
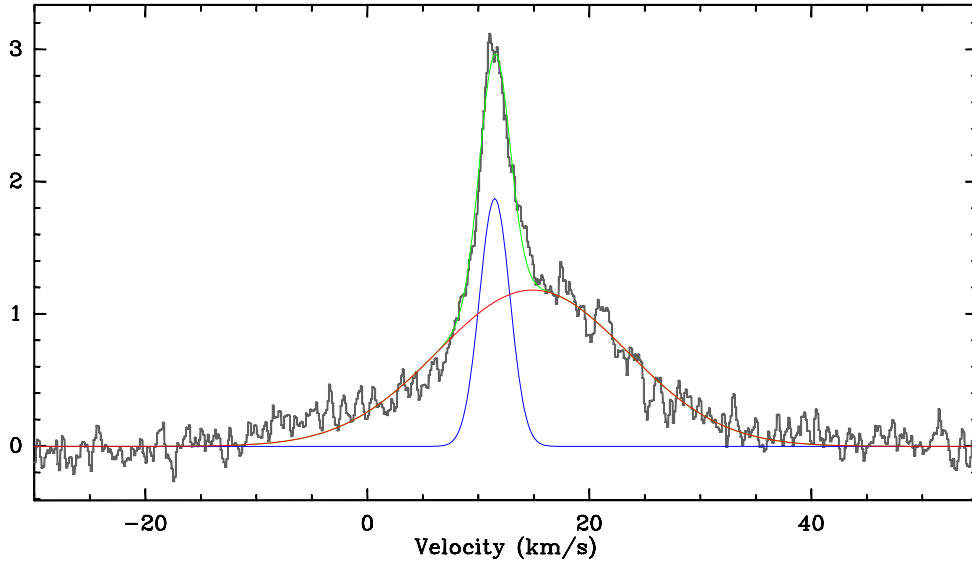

Figure 3.15: Spectrum of the ^{12}CO (10–9) transition (grey) of the intermediate–mass Vela 19, with a two Gaussian fit (green). The fit there are a narrow component, 3.2 km s^{-1} FWHM, centered at 11.5 km s^{-1} (blue), and a broader component, 20.6 km s^{-1} FWHM, situated at 14.7 km s^{-1} (red).

Table 3.2: Integrated intensity, peak temperature, widths two Gaussian fit and rms for each detected ^{12}CO (10–9) line.

Source	$\int T_{MB}dV$ (K km s^{-1})	T$_{peak}$ (K)	FWHM^b (km s^{-1})	FWHM^c (km s^{-1})	rms^a (K)
Low–mass					
L 1448-MM	8.61	1.42	12.91	1.64	0.147
NGC 1333 IRAS 2	7.08	2.13	5.51	1.54	0.089
NGC 1333 IRAS 4A	37.10	1.62	21.33	2.20	0.084
NGC 1333 IRAS 4B	25.15	2.67	16.21	3.32	0.087
L 1527	4.22	1.53	9.34	1.81	0.074
BHR 71	7.53	0.76	24.76	2.48	0.091
L 1157	7.89	0.64	13.33	1.82	0.092
L 1489	3.96	0.73	9.41	2.19	0.113
L 1551 IRS 5	13.23	3.03	14.92	2.52	0.085
TMC 1	5.81	1.38	4.12	1.38	0.076
IRAS 12496/HH54	7.80	1.93	3.94	1.51	0.089
Ced110 IRS4	4.20	1.48	2.44	1.17	0.103
Intermediate mass					
NGC 7129 FIRS 2	24.23	1.91	20.93	5.31	0.089
L1641 S3 MMS1	24.66	2.07	17.61	5.73	0.083
NGC 2071	347.57	22.07	21.59	7.04	0.198
Vela IRS 17	75.97	11.75	15.22	4.59	0.078
Vela IRS 19	33.64	3.07	18.39	3.50	0.116

^{a} In 0.26 km s^{-1} bins.

^{b} Broad component.

^{c} Narrow component.

Table 3.3: ^{13}CO (10–9) emission obtained from Gaussian fits. The values showed are the integrated intensity, the peak temperature, the width(s) and the rms.

Source	$\int T_{MB}dV$ (K km s^{-1})	T$_{peak}$ (K)	FWHM[b] (km s^{-1})	FWHM[c] (km s^{-1})	rms[a] (K)
Low–mass					
L 1448-MM	0.24	0.11	1.77	–	0.018
NGC 1333 IRAS 2	0.60	0.21	2.37	–	0.019
NGC 1333 IRAS 4A	1.16	0.08	12.94	–	0.023
NGC 1333 IRAS 4B	0.71	0.10	6.28	–	0.019
BHR 71	0.34	0.20	1.85	–	0.017
L 1157	–	–	–	–	–
L 1489	0.44	0.05	7.31	–	0.025
L 1551 IRS 5	1.26	0.53	2.50	–	0.025
TMR 1	0.35	0.08	3.23	–	0.028
HH 46	0.28	0.10	1.89	–	0.028
IRAS 12496/HH54	0.76	0.15	4.51	–	0.028
Ced110 IRS4	–	–	–	–	–
Intermediate mass					
NGC 7129 FIRS 2	0.51	0.11	4.54	–	0.022
L1641 S3 MMS1	1.11	0.26	9.76	2.84	0.052
NGC 2071	15.29	2.41	11.57	3.99	0.020
Vela IRS 17	4.15	1.05	3.91	–	0.126
Vela IRS 19	4.57	1.01	6.77	6.60	0.090
High mass					
W3-IRS5	124.59	19.71	15.10	4.82	0.027
NGC7538-IRS1	39.35	7.53	8.75	3.53	0.023
DR21(OH)	50.04	6.73	16.02	5.82	0.026
AFGL2591	27.71	6.50	6.95	3.04	0.019
IRAS05358+3543	6.14	0.91	15.40	3.77	0.019
NGC6334-I(N)	13.6	1.99	12.60	4.34	0.027
NGC6334-I	56.11	8.12	21.32	5.51	0.075
W51N-e1	65.63	6.61	15.23	6.52	0.100
G34.26+0.15	52.80	8.1	12.55	5.09	0.116
W33A	10.40	1.63	11.77	3.55	0.018
G31.41+0.31	17.69	2.63	6.36	–	0.106
W43-MM1	4.41	0.84	5.32	–	0.169
G29.96−0.02	31.61	5.36	13.54	4.67	0.108

[a] In 0.27 km s^{-1} bins.
[b] Broad component.
[c] Narrow component.

Table 3.4: $C^{18}O$ (5–4) emission obtained from Gaussian fits in each detected source. The values are the integrated intensity, the peak temperature, the width(s) and the rms.

Source	$\int T_{MB}dV$ (K km s^{-1})	T_{peak} (K)	FWHM[b] (km s^{-1})	FWHM[c] (km s^{-1})	rms[a] (K)
Low−mass					
L 1448-MM	0.42	0.42	3.13	0.71	0.004
NGC 1333 IRAS 2	0.85	0.72	1.32	0.71	0.004
NGC 1333 IRAS 4A	0.53	0.45	2.04	1.04	0.005
NGC 1333 IRAS 4B	0.38	0.15	1.80	−	0.004
L 1527	0.54	0.46	2.69	0.55	0.004
BHR 71	0.67	0.55	1.64	0.62	0.005
L 1157	0.19	0.14	0.76	−	0.004
Ser SMM 4	1.53	0.61	4.54	1.89	0.004
Ser SMM 1	1.84	1.07	3.15	1.25	0.004
Intermediate mass					
NGC 7129 FIRS 2	0.50	0.19	7.11	2.03	0.004
L1641 S3 MMS1	0.78	0.45	1.73	−	0.023
NGC 2071	7.10	1.83	7.54	2.26	0.005
Vela IRS 17	5.15	1.35	8.72	3.59	0.034
Vela IRS 19	1.95	0.53	9.46	2.58	0.009

[a] In 0.27 km s^{-1} bins.
[b] Broad component.
[c] Narrow component.

.

Table 3.5: Integrated intensity, peak temperature, width and rms obtained from the one single Gaussian fit of each detected $C^{18}O$ (10–9) line, for the different types of YSOs.

Source	$\int T_{MB}dV$	T_{peak}	FWHM	rms[a]
	(K km s^{-1})	(K)	(km s^{-1})	(K)
Low−mass				
L 1448-MM	–	–	–	–
NGC 1333 IRAS 2	0.18	0.07	2.32	0.020
NGC 1333 IRAS 4A	–	–	–	–
NGC 1333 IRAS 4B	–	–	–	– -
Intermediate mass				
NGC 7129 FIRS 2	–	–	–	–
High mass				
W3-IRS5	14.81	3.41	4.06	0.149
NGC7538-IRS1	3.73	0.91	3.83	0.055
DR21(OH)	7.44	1.16	6.27	0.026
AFGL2591	3.11	0.93	3.31	0.031
NGC6334-I(N)	1.77	0.35	5.85	0.026
NGC6334-I	8.16	1.58	4.96	0.030
W51N-e1	10.11	1.51	6.44	0.060
W33A	1.55	0.30	4.79	0.031
W43-MM1	0.63	0.12	5.07	0.029
G29.96−0.02	5.16	1.04	4.67	0.043
IRAS05358+3543	0.51	0.11	4.26	0.063

[a] In 0.27 km s^{-1} bins.

Table 3.6: $C^{18}O$ (9–8) emission obtained from Gaussian fits in each detected source. The values are the integrated intensity, the peak temperature, the width(s) of and the rms.

Source	$\int T_{MB}dV$ (K km s^{-1})	T$_{\text{peak}}$ (K)	FWHM[b] (km s^{-1})	FWHM[c] (km s^{-1})	rms[a] (K)
Low−mass					
NGC 1333 IRAS 2	0.18	0.07	2.31	−	0.020
Ser SMM 1	0.53	0.14	3.35	−	0.022
L 1551 IRS 5	0.43	10.10	3.24	−	0.021
Elias 29	0.40	0.08	4.68	−	0.024
GSS 30 IRS1	0.19	0.06	2.82	−	0.021
Intermediate mass					
NGC 7129 FIRS 2	−	−	−	−	−
L1641 S3 MMS1	−	−	−	−	−
NGC 2071	2.63	0.54	9.21	2.61	0.024
Vela IRS 17	0.59	0.17	2.83	−	0.021
Vela IRS 19	0.40	0.11	3.15	−	0.024
AFGL 490	0.45	0.06	6.01	−	0.022
High mass					
W3-IRS5	22.70	5.01	4.32	−	0.049
NGC7538-IRS1	6.33	1.4	4.23	−	0.043
DR21(OH)	9.21	1.66	5.63	−	0.064
AFGL2591	4.46	1.30	3.31	−	0.043
NGC6334-I(N)	1.72	0.46	4.24	−	0.065
NGC6334-I	11.81	2.15	5.31	−	0.067
W51N-e1	14.01	2.02	6.70	−	0.046
G34.26+0.15	15.69	2.6	5.60	−	0.060
W33A	2.42	0.53	5.07	−	0.040
G31.41+0.31	5.11	0.89	6.31	−	0.044
W43-MM1	1.93	0.31	6.06	−	0.039
G29.96−0.02	7.10	1.50	4.52	−	0.042
IRAS05358+3543	0.91	0.26	3.92	−	0.045
G327−0.6	5.61	0.90	6.26	−	0.053
IRAS16272−4837	1.06	0.14	6.83	−	0.047

[a] In 0.30 km s^{-1} bins.

[b] Broad component.

[c] Narrow component.

4

Analysis

From the CO and isotopologue line profiles of the observed YSOs, some observational parameters have been obtained, like the integrated intensity, the peak main beam temperature and the FWHM for different profile components. However, a further analysis is still necessary in order to get more information about the sources. Therefore, this chapter presents correlations performed on the data and an analysis of the optical depth, with the aim of finding a connection among the different types of YSOs.

4.1   Correlations

In order to examine similarities and differences among the three types of YSOs in a systematic manner, the integrated line flux, W, is compared to various key physical properties of the observed sources and general trends are explored. The more important outcomes are presented in Figs. 4.1 to 4.5. One of these key properties is the bolometric luminosity, L_{BOL} of an object, which is an indication of the mass of the protostar. Another important value is the integrated intensity of a spectral line. For an emission profile, this value can be used to calculate the column density of a specific molecule, assuming the population distribution is in local thermal equilibrium (LTE) at a single temperature. The integrated intensity of the line, W, decreases with distance, because it is proportional to the flux at that frequency and this magnitude is defined as $F_\nu = L_\nu/(4\pi d^2) \sim W$. The parameter d is the distance at which the sources is and L_ν its luminosity for that specific frequency ν. Therefore, in order to perform a proper comparison among the results obtained in the previous chapter, (Tables 3.2 to 3.6), the integrated intensities of the emission lines were normalized to a common distance of 1 kpc, a representative distance for both low–, intermediate– and high–mass YSOs.

Using those parameters, one of the goals is to characterize how the intensity of the radiation coming from a source, as originating from a specific molecule and energy

transition, varies with the bolometric luminosity of that source. The study will be extended through the three types of YSOs, that is, objects with different mass. Therefore, for each detected line, a representation of the normalized integrated intensity, W, versus the $L_{\rm BOL}$ has been performed.

4.1.1 ^{12}CO (10-9)

Figure 4.1 shows the correlation for the ^{12}CO (10–9) lines. It is seen that most of the values are distributed along a straight line, which is determined from a linear fit and defined as: $\log W = a + b \cdot \log L_{\rm BOL}$. The slope and the y–intercept of the line are $b = 0.98{\pm}0.11$ and $a = -1.23{\pm}0.17 \log({\rm K\,km\,s}^{-1}\,L_{\odot}^{-b})$, respectively. Luminosity and ^{12}CO line strength are proportional, since $b \sim 1$, so it is possible to make the approximation where $W \sim 10^{-1.23} \cdot L_{\rm BOL}$, that is, $W \sim 0.06 \cdot L_{\rm BOL}$. This result extends over more than three orders of magnitude.
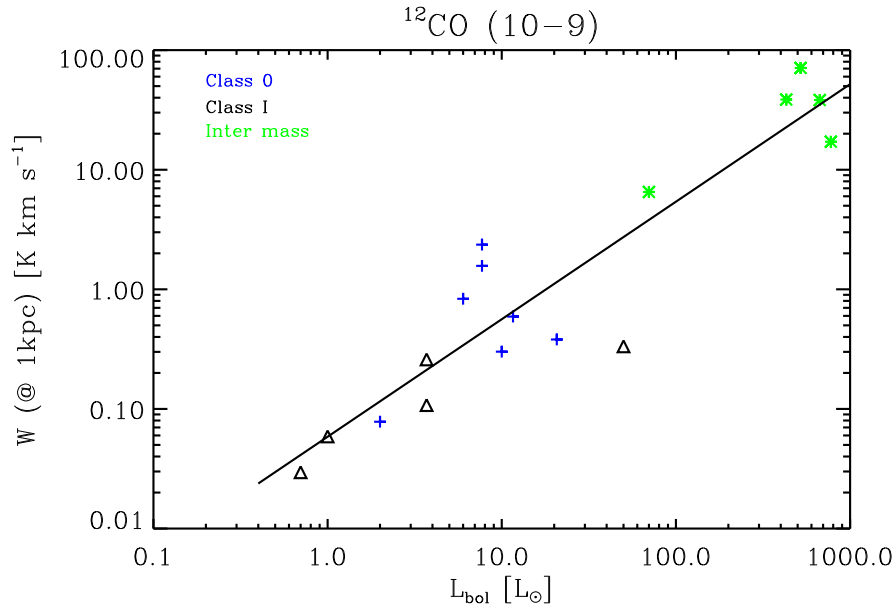

Figure 4.1: The integrated intensity of the ^{12}CO (10–9) lines detected in different types of YSOs normalized to a distance of 1 kpc versus the bolometric luminosity of those sources.

Even if most of the line intensities of the observed LM and IM sources fit quite well to a straight line, there are three LM sources which stand out. Two of those are the class 0 objects with the most intense emission line profile and with strong outflows, that is, NGC1333 IRAS4A and IRAS4B (e.g. Yıldız et al., in prep.). The other source, IRAS12496, is the class I with the highest $L_{\rm BOL}$. Comparing the value of its luminosity with that of some IM objects, IRAS12496 can be considered on the border between the low and intermediate type YSO. However, the reasons why

this source does not follow the correlation as good as the other class I protostars are probably related to other factors, like its evolutionary stage or its orientation to the observer. IRAS12496 is classified as a class I/II object, becoming the most evolved source of the low–mass sample. Besides, the central source is easier to see since one of its outflows is pointing towards us. Those are some of the reasons justifying why its observational characteristics differ considerably from other low–mass YSOs. Nevertheless, the existence of a correlation between these parameters is quite evident and followed by the two types of YSOs.

4.1.2 ^{13}CO (10-9)

For the case of ^{13}CO (10–9) lines, values from the HM sources are added. Therefore, it will be possible to investigate if this specific behaviour and relation also holds for higher mass sources. The correlation of this CO isotopologue is presented in Figure 4.2.
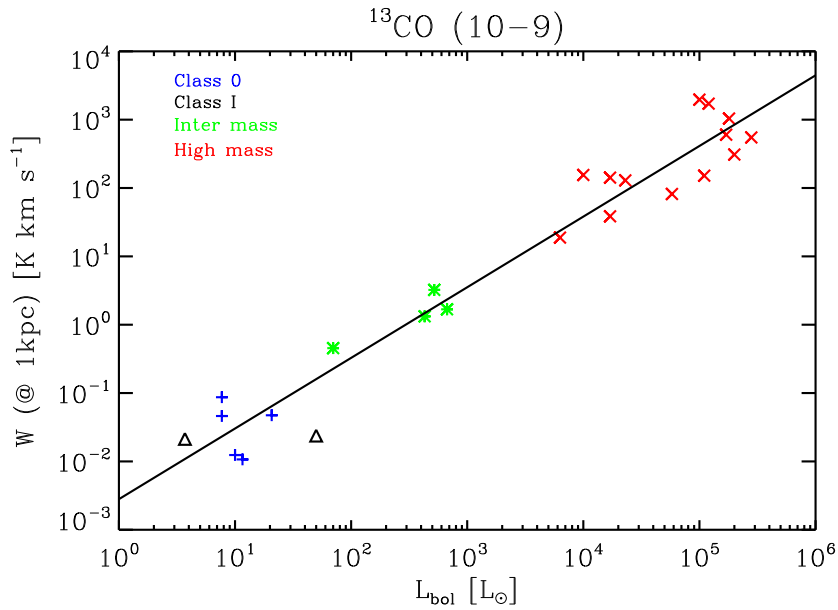

Figure 4.2: The integrated intensity of the ^{13}CO (10–9) lines detected in different types of YSOs normalized to a distance of 1 kpc versus the bolometric luminosity of those sources.

The emission lines at this frequency are weaker than those detected at the ^{12}CO (10–9) transition. This result is not surprising because the abundance ratio between ^{12}C and ^{13}C is approximately 65, i.e, ^{12}C/^{13}C ~ 65, and obviously that ratio is the same for ^{12}CO and ^{13}CO. Therefore, the calculated values of the W for the ^{13}CO lines entails higher noise and more uncertainty. Despite this, a clear correlation is also found across the different types of YSOs at this frequency. Hence, the obtained values can be

fitted properly by one linear relation, finding again that the class I source IRAS12496 appears further from the calculated straight line. The characteristic parameters of the applied linear fit, slope and y–intercept of the line are $b = 1.03 \pm 0.05$ and $a = -2.55 \pm 0.19 \log(\mathrm{K\,km\,s^{-1}}\, L_\odot^{-b})$, respectively. Comparing with the values obtained for the ^{12}CO (10–9) correlation, it is seen that both slope parameters are practically the same, so adding the HM sources does not modify it. This also means that the luminosity and ^{13}CO line strength are virtually proportional, so $W \sim 0.003 \cdot L_{\mathrm{BOL}}$ However, the y–intercept value is smaller for ^{13}CO (10–9), due to the explained different abundances, giving smaller values of the integrated intensities for those lines.

4.1.3 C^{18}O (5-4), (9-8) and (10-9)

The emission lines of this isotopologue, and therefore their integrated intensities, are weaker than the ones obtained for the ^{12}CO molecule. The reason is related to the abundance ratio existing, this time, between ^{16}O and ^{18}O. The value of this ratio is ~ 550, which means that C^{16}O/C^{18}O$\sim$550.

In the representation of the normalized W for the C^{18}O (5–4) lines versus the sources L_{BOL}, only low–mass class 0 and intermediate–mass objects are presented. Therefore, the available data is more limited than in previous representations. Nevertheless, a correlation is found (Figure 4.3). The obtained results fit quite well to a straight line given by the formula already indicated: $\log W = a + b \cdot \log L_{\mathrm{BOL}}$. The y–intercept of the line is $a = -2.25 \pm 0.14 \log(\mathrm{K\,km\,s^{-1}}\, L_{\mathrm{BOL}})$, is smaller than the value determined for the ^{12}CO (10–9) linear fit, due to the different abundances between C^{16}O and C^{18}O. The slope is $b = 0.84 \pm 0.08$, becoming the smallest value obtained for this parameter in this analysis. In this case, only one source, Ser SMM4, is located far from the straight line. Removing this LM object from the fit, the slope achieved is closer to 0.99, showing then the same behaviour as the previous studied transitions and isotopologues.

In order to continue with the search of correlations and relations among the different types of YSOs, the analysis of the C^{18}O (9–8) lines will be carried out as well. For this CO isotopologue transition, results from HM sources are added but only four LM sources are detected, being the weakest one of the total sample. Figure 4.4 shows the correlation for the values obtained at this frequency, fitted by a first order polynomial.

The behaviour followed by the IM sources is practically the same at any frequency, that is, the results obtained for those objects were quite similar in all the calculated correlations, finding these YSOs close to the linear fit. However, comparing the values obtained for the HM sources at this frequency with those for the ^{13}CO (10–9) line, an interesting difference is found. For the C^{18}O (9–8) transition, the calculated values for the high–mass sources are more spread. The reason could be related to
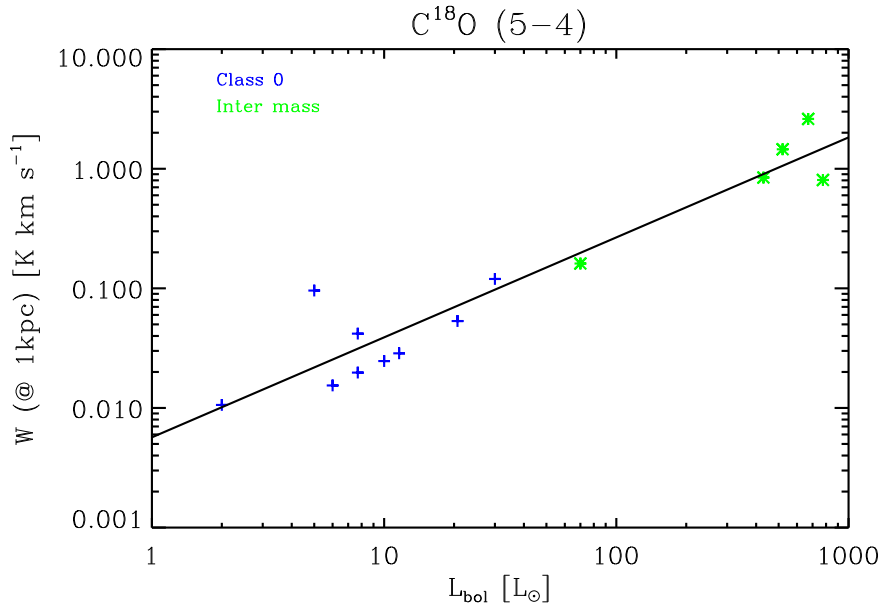
Figure 4.3: The integrated intensity of the $C^{18}O$ (5–4) lines detected in different types of YSOs normalized to a distance of 1 kpc versus the bolometric luminosity of those sources.

the fact that at this frequency, the emission lines are weak and the baseline shows some structures, like ripples close to the line of interest, which can underestimate or overestimate the values of the integrated intensity. However, a linear fit was applied, where the characteristic parameters are: $b = 1.07 \pm 0.08$ for the slope of the line, and $a = -3.5 \pm 0.3 \log(\text{K km s}^{-1} L_\odot^{-b})$ for the y–intercept.

The $C^{18}O$ (10–9) line is only detected in high–mass source, limiting the number of data points in Figure 4.5. Similar to what was shown for the $C^{18}O$ (9–8) transition, these values appear quite spread out. Even if they can be fitted by a straight line, the errors of the parameters which define the line are the highest ones obtained.

For these spectra, the calculation of the integrated intensity was the most difficult one since there is a strong water line close to this specific emission line. In addition, since there is no detection of lines originating in other types of YSOs, this cannot be considered a really useful correlation (in order to compare results through different mass values). Nevertheless, a linear fit was performed and the characteristic parameters are $b = 0.9 \pm 0.4$ for the slope and $a = -2.9 \pm 1.7 \log(\text{K km s}^{-1} L_\odot^{-b})$ for the y–intercept.

Therefore, a correlation is observed among the different types of YSOs and for all their detected CO and isotopologues lines. Those correlations are very similar, as the
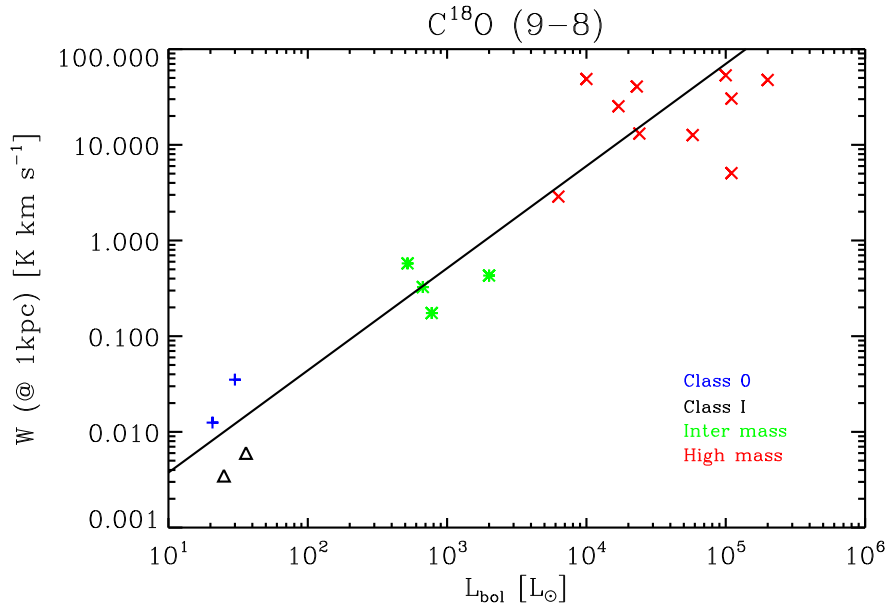
Figure 4.4: Representation of the normalized integrated intensity calculated from the $C^{18}O$ (9–8) lines detected in different high mass sources vs the L_{BOL} of those sources.

values obtained for the slope and the y–intercept of the linear fits show.

4.1.4 Multiple components in ^{12}CO line profiles

The same representation has been carried out for each component in which the ^{12}CO (10–9) emission line profiles can be decomposed. The characteristic multiple–component profile has been already found in some water lines profiles and its classification and explanation was presented in the previous chapter. Therefore, the broad and medium–broad components identified in those lines has been studied separately and its integrated intensity, W, calculated (Table 3.1), aiming to accomplish a deeper understanding of these structures.

The correlation obtained for the medium–broad component is presented in Figure 4.6. The integrated intensities are greater than those calculated for the narrow ones. This means that most of the contribution to this parameter is given by the broad–medium components, that is, by the shocks created by the outflows. This contribution is even more important and bigger for the spectra of the low–mass sources, the value of W of those components is at least 3 times the values obtained for the narrow ones. For the intermediate–mass objects, the differences are smaller and W of the broad components are around twice the values calculated for the narrower components. This predominance of the broad–medium components is also seen in the distribution of the values along the relation. The correlation for the broad profile is
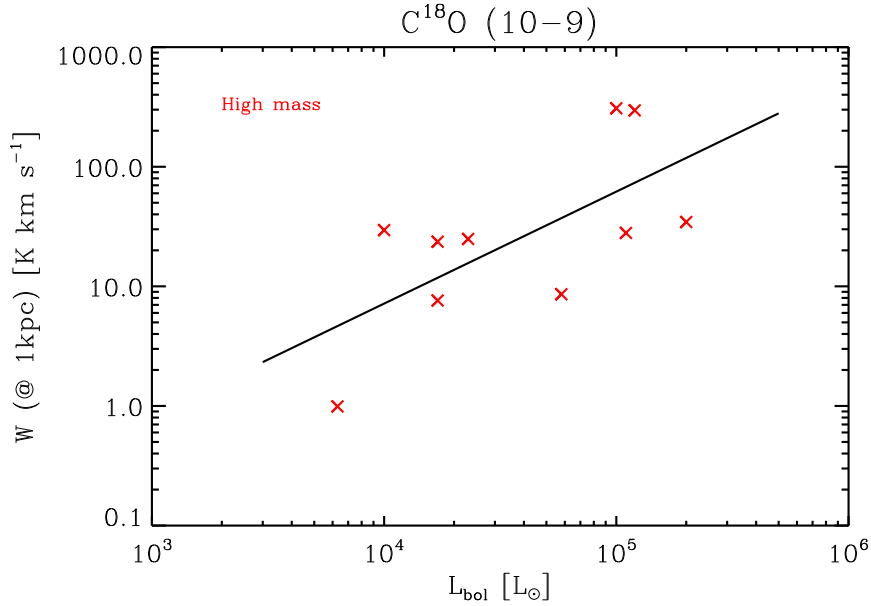
Figure 4.5: Representation of the normalized integrated intensity (1 kpc) of the $C^{18}O$ (10–9) lines detected in different types of YSOs versus the bolometric luminosity of those sources.

more similar to that obtained for the full profile (Figure 4.1). A linear fit is properly applied and the fit parameters are similar to the previous values, where again, the LM source IRAS12496 is the one that appears further from the fit. The parameters of the straight line are $b = 0.96 \pm 0.15$ for the slope and $a = -1.4 \pm 0.3$ $\log(\mathrm{K\,km\,s^{-1}}\,L_\odot^{-b})$ for the y–intercept of the line.

The correlation of the narrow components is presented in Figure 4.7. The data are better fitted by a straight line than those obtained from the broad–medium components. However, there is a source whose integrated intensity is the smallest one of the sample, and it does not follow the W–L_{BOL} correlation. This is the LM object BHR 71 and looking at its spectrum, a weak and small narrow component is hardly identifiable in the line profile. The parameters of the linear fit are in this case: $b = 0.97 \pm 0.12$ for the slope and $a = -1.7 \pm 0.2$ $\log(\mathrm{K\,km\,s^{-1}}\,L_\odot^{-b})$ for the y–intercept of the line. Since their integrated intensity values are smaller than those obtained for the broad–medium components, the y–intercept value is also smaller than the one calculated in the previous correlation.

In order to compare easily the parameters of the linear fits for each line, they are presented (which their errors) in Table 4.1. One of the highlighted result was the similar values for the slope, indicating a proportional relationship between the luminosity and the integrated intensity of the specific observed line. The y–intercept is used to obtain the constant which relates both magnitudes by the value 10^a.
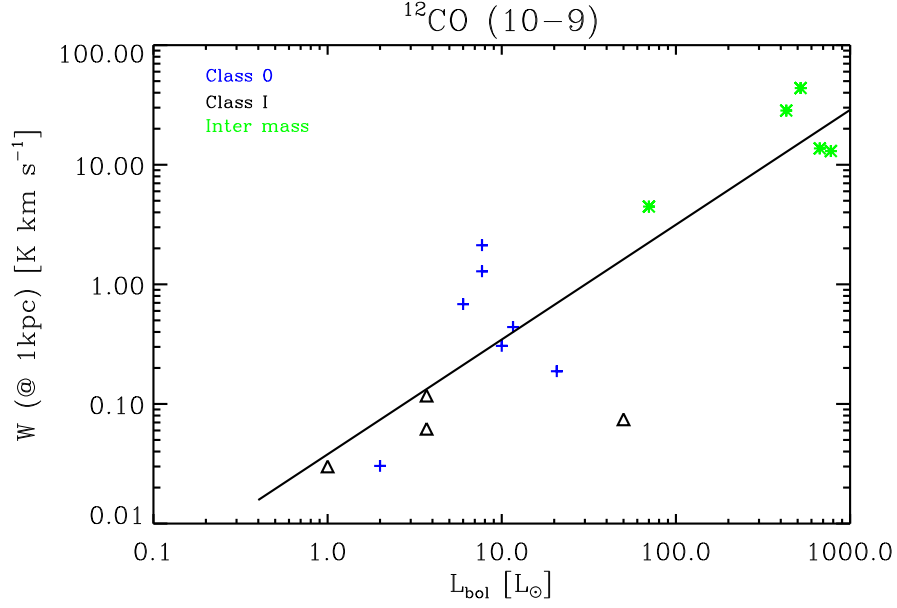
Figure 4.6: Representation of the normalized integrated intensity (at 1 kpc) of the broad component identified in the ^{12}CO (10–9) lines for different types of YSOs versus the bolometric luminosity of those sources.

Table 4.1: Slope and y–intercept of the calculated linear fit for each CO and isotopologue line. The fitted equation is $\log W = a + b \cdot \log L_{\mathrm{BOL}}$.

Line	a	$\sigma(a)$	b	$\sigma(b)$
^{12}CO (10-9)	-1.23	0.17	0.98	0.11
^{13}CO (10-9)	-2.55	0.19	1.03	0.05
C^{18}O (5–4)	-2.25	0.14	0.84	0.08
C^{18}O (9–8)	-3.5	0.3	1.07	0.08
C^{18}O (10–9)	-2.9	1.7	0.9	0.4
^{12}CO (10-9)[c]	-1.4	0.3	0.96	0.15
^{12}CO (10-9)[d]	-1.7	0.2	0.97	0.12

[c] Broad component.
[d] Narrow component.

4.2   Optical depth

The description of how transparent a cloud (or a stellar/planetary atmosphere) is to radiation travelling through it is given by the optical depth, τ. This parameter is the dimensionless e-folding factor for absorption of hot radiation through a cooler gas layer. The fraction of intensity absorbed per unit length is defined by the opacity,
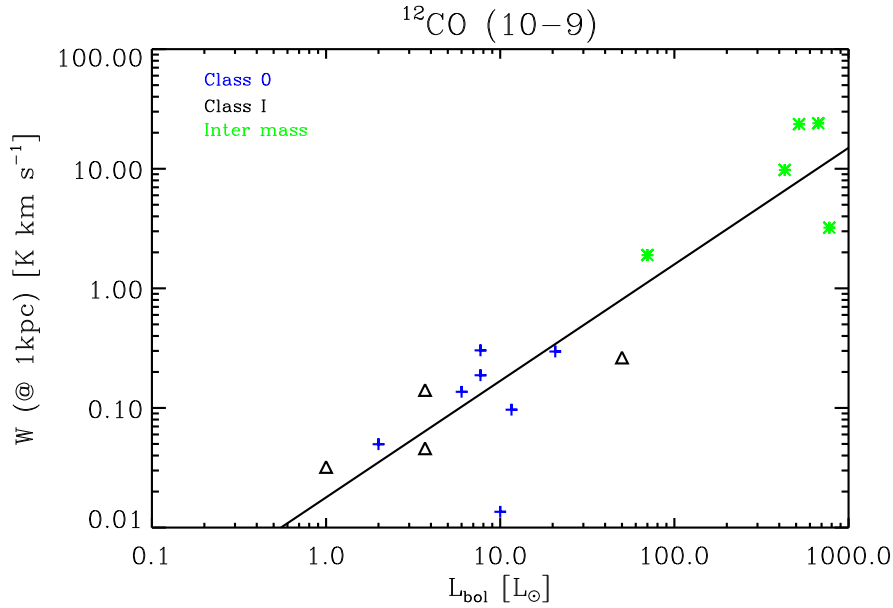
Figure 4.7: Representation of the normalized integrated intensity of the medium–broad component identified in the ^{12}CO (10–9) lines for different types of YSOs versus the bolometric luminosity of those sources.

κ_ν, value which depends on the frequency, temperature, etc. Therefore, the optical depth is related to the opacity and the equation which shows that relation (for a one–dimensional path s) is: $d\tau_\nu(s) = -\kappa_\nu(s)ds$. For instance, τ also depends on the frequency and the path. Integrating the previous expression for a certain s, the total optical depth is obtained. If τ is < 1, the cloud is optically thin, which means that a photon can travel that distance s without being absorbed or scattered. The opposite situation, when τ is > 1, is known as optically thick.

Considering a cool cloud with a temperature gradient increasing through its center, where a hot source of radiation is, the system can be divided in different layers, characterized by being in local thermal equilibrium, LTE. If in one of those layers, with a specific temperature and situated a distance S from the cloud edge, the existing molecules are emitting radiation (de–excitation process), the beam of radiation will enter the next layer with an intensity I_{in}. However, part of the intensity will be absorbed by passing through the cloud. Assuming that the cloud itself provides negligible emissivity, that is, the emission from the remainder layers is not considered, then the drop in intensity of the beam of radiation is: $dI = -\kappa_\nu(s)Ids$. The parameter I is the intensity entering each volume element and ds the length of each layer. Therefore, the intensity measured out of the cloud, $I_{\text{out}}(s = 0)$, will be:

$$I_{\text{out}} = I_{\text{in}} \cdot e^{(-\int_S^0 \kappa_\nu ds)} = I_{\text{in}} \cdot e^{-\tau_\nu} \tag{4.1}$$

In order to estimate the CO optical depth, Equation 4.1 will be used and lines from two different isotopes are needed. In addition, some assumptions must be considered: LTE and same value of the excitation temperature for both species. Therefore, in this subsection, the determination of this parameter for different YSOs will be performed using the J=10–9 lines of ^{12}CO and ^{13}CO. To achieve this goal, another factor is necessary, the isotopic abundance ratio of both species, r. For ^{12}CO and ^{13}CO, this value is $r = x(^{12}\text{CO})/x(^{13}\text{CO}) \sim 65$ (Langer & Penzias 1990). Thus, assuming ^{13}CO J=10–9 lines are optically thin, the ^{12}CO/^{13}CO intensity ratio is given by the abundance ratio r=65. This factor is then interpreted as the theoretical emission intensity of ^{12}CO, that is, the beam of radiation originating in the aforementioned layer and defined as the incident intensity I_{in}. Therefore, the observed intensity, I_{out}, is obtained dividing the central temperature peak of the detected ^{12}CO (10–9) lines over the central temperature peak of the corresponding ^{13}CO (10–9) lines of those sources observed in both frequencies. These values are presented in the third column of Tables 3.2 and 3.3, respectively.

Since the ratios are calculated with the observed data described in the result chapter, I_{out} is known and I_{in} is the assumed theoretical value, I_{theor}=65, Then, the optical depth can be obtained from equation 4.1 as:

$$\tau = \ln\left(\frac{I_{\text{theor}}}{I_{\text{out}}}\right) \tag{4.2}$$

The estimated values for the YSOs with emission detected for both species are presented in Table 4.2. The highest optical depth is 2.73, achieved by BHR 71, and the lowest one is 0.95, for NGC 1333 IRAS 4B. Looking at the results, only in this last source is the CO (10–9) optically thin. For the other objects, since τ is > 1, the CO (10–9) lines are considered optically thick at the line center.

Table 4.2: Summary of the calculated optical depth for some detected ^{12}CO (10–9) lines.

Low–mass	τ_ν	Intermediate–mass	τ_ν
L 1448-MM	1.65	NGC 7129 FIRS 2	1.35
BHR 71	2.73	L1641 S3 MMS1	1.91
NGC 1333 IRAS 2	1.97	NGC 2071	1.95
NGC 1333 IRAS 4A	1.14	Vela IRS 17	1.68
NGC 1333 IRAS 4B	0.95	Vela IRS 19	1.56
L 1551 IRS 5	2.27		
L 1489	1.58		
IRAS 12496/HH54	1.67		

5

Conclusions

Throughout this report, high–J CO observations performed by the HIFI spectrometer have been analyzed for a varied sample of 43 young stellar objects. These sources represent a wide range of luminosity and mass values, being able to trace and compare, for the first time, the characteristics and properties of the CO and some isotopologues emission lines across the entire mass spectrum. Using just the present ground–based telescopes, the observations of these high transitions are impossible. However, thanks to the *Herschel* Space Observatory, the sub–millimetre window is now accessible and the science behind it can be discovered. Therefore, one of the goals of this thesis is to start exploring that window in order to achieve a deeper understanding of the star–forming regions, places where complicate physical and chemical processes are carried out. For this reason, a preliminary study among the different types of YSOs was performed through their spectra, trying to find a link from the low– to the high–mass sources by comparing their main observable characteristics.

After introducing some of the most important concepts and aspects related to YSOs (classification, WISH key program, CO observations), and describing the telescope and instrument used, the sample of sources and lines of interest were presented. Established the proper background, the next step was to analyze the data and obtain the most characteristic and defining features of the detected emission lines for the available range of luminosities and masses.

Most of the profiles showed a high S/N, with strong and well defined lines, above all, the ^{12}CO (10–9) lines and those from the HM sources. During their characterization, some structures were identified in the profiles, such as bullets (EHV components) or self–absorption features. These latter ones were only significant enough within the noise in the spectra of the high–mass sources. However, the most highlighted feature was the presence of multiple components, found in some line profiles. These structures have been already identified in different water lines, so the obtained results will be used as a complement of the water observations in future work. The identifica-

tion of multiple emission components involves the existence of shocks, created in the outflow cavity walls (broad component) and in the inner dense envelope (medium component). These shocks can cause important effects on the different protostar environments (outflows, disk, envelope) modifying their physics and chemistry. The ^{12}CO (10–9) lines are the ones that showed the clearest and most evident multiple component profile, so a deeper analysis of these spectra was carried out, involving the calculation of specific values such as the integrated intensity and the peak temperature for each component. Two are the components identified, classified as broad–medium and medium (narrow). However, these structures are narrower than those found in the water lines profiles, so the comparation and analysis of these two results (for CO and H$_2$O) should be performed carefully. The reason why the components of the ^{12}CO (10–9) line profiles are narrower is still in debate but it could mean that we are looking at deeper areas of the protostar, so smaller regions are being observed (regarding to the size of the entire system) and that is reflected on the width of these components.

The analysis continues with the calculation of different observational parameters, such as the integrated intensity (W), FWHM and peak temperature, for the emission lines of the observed sources. Then, a correlation between the integrated intensity (normalized to 1 kpc) and a key physical parameter, the bolometric intensity (L_{BOL}), was looked for. The aim was to find a relationship among some magnitudes which characterize a system and also along the entire mass spectrum. Considering the figures and fits obtained in chapter 4, it is seen that most of the values are distributed along a straight line, defined as $\log W = a + b \cdot \log L_{\text{BOL}}$. Therefore, a correlation is found between W and L_{BOL}, extending it through 3 order of magnitude. For all the CO and isotopologue lines, the slope of the fitted line, b, is ~ 1, which means that the strength of the line is practically proportional to the bolometric luminosity. Therefore, for these frequencies, the relation between these two parameters can be written as: $W \sim C \cdot L_{\text{BOL}}$, where $C = 10^a$. The values of C depends on the y–intercept, which is related to the intensity of the lines, that is, with the amount of that specific species (given by the abundance ratio r). In chapter 4 are highlighted the sources which do not follow the correlation, being IAS12496 the one that more often stands out from the linear fit. In addition, this relation was also performed for each of the components identified in the ^{12}CO (10–9) line profiles. The representations show that the broad–medium components are the one that prevail since their values are distributed in a similar way to those obtained for the full profile. On the other hand, the medium components are fitted by a straight line better than the broad–medium components, following clearly the aforementioned correlation.

In the analysis section, an important quantity, the optical depth (τ), was calculated using the results presented in chapter 3. Since this parameter can be only calculated in different species for the same energy transition, it was obtained just for the ^{12}CO (10–9) emission line profiles. All sources (low– and intermediate–mass

YSOs) present a value which corresponds to optically thick line in its central position. However, a deeper analysis should be developed, comparing again the values obtained from the multiple component profiles and also for other lines, as $C^{18}O$ (10–9) line profiles. Part of this future work will be also to calculate other quantities such as the column density or the excitation temperature for a specific species, being able to characterize the protostar system and their different structures.

Therefore, this thesis has focused on the description of the main features presented in the different detected line profiles for the observed YSOs. The aim was to characterize them and find similarities, differences and correlation along the wide mass range considered, since these lines have not been observed before. The preliminary analysis performed shows the existence of a correlation between the integrated intensity of the line and the bolometric luminosity of the source and also it classifies the ^{12}CO (10–9) lines as optically thick in its central position. However, these are just preliminary conclusions since a further analysis will be carried out with the results presented in this thesis and with the incoming data still expected. These future results and conclusions will complement those already obtained for other molecules, such as water, getting a global description of the protostar system. In addition to the observational data, radiative modeling will be also developed to understand some phenomena, such as the shocks, but basically the physics and chemistry of the young stellar objects.

Complementing the research, other activities were carried out. In September I could assist to the *5th Zermatt Symposium*, where the conditions and impact of the star formation, through the first results of *Herschel* were presented. This was an incredible opportunity to know the different key programs, focused on distinct aspect of the star formation, and the results obtained by those groups. Also, a WISH team meeting took place during that week and part of the obtained results showed in this thesis were presented. Finally, I could observe during 6 night at the 15 m in diameter telescope James Clerk Maxwell Telescope (JCMT) situated in the summit of Mauna Kea (4092 m), Hawaii. None of these observed data could be included in this project because the run finished on December 2. However, the data will be use during the next months, as a continuation of the work done during these previous 4 months. The purpose of these observations was to map seven low–mass YSOs at different evolutionary stage in HCN and CN since these species are excellent tracer of the UV fields. The UV fields are originated near the protostar and they illuminate the walls created by the outflows. Therefore, these observations will provide more information about the different components of the YSO and they will help to develop accurate radiative models which explain how shocks are created, the influence of the outflows over the envelope and basically how the chemistry is affected by these violent phenomena. Thus, these complementary activities are part of the PhD preparation, highlighting the latter one since this experience taught me the procedures needed to observe in other similar telescopes as IRAM 30m or APEX.

References

Andre, P., Ward-Thompson, D., & Barsony, M. 2000, Protostars and Planets IV, 59

Bachiller, R. & Tafalla, M. 1999, in NATO ASIC Proc. 540: The Origin of Stars and Planetary Systems, ed. C. J. Lada & N. D. Kylafis, 227–+

Bruderer, S., Benz, A. O., Stäuber, P., & Doty, S. D. 2010, ApJ, 720, 1432

Chavarría, L., Herpin, F., Jacq, T., et al. 2010, A&A, 521, L37+

Crimier, N., Ceccarelli, C., Alonso-Albi, T., et al. 2010, A&A, 516, A102+

de Graauw, T., Helmich, F. P., Phillips, T. G., et al. 2010, A&A, 518, L6+

Evans, N. J., Dunham, M. M., Jørgensen, J. K., et al. 2009, ApJS, 181, 321

Fuente, A., Neri, R., & Caselli, P. 2005, A&A, 444, 481

Griffin, M. J., Abergel, A., Abreu, A., et al. 2010, A&A, 518, L3+

Johnstone, D., Fich, M., McCoey, C., et al. 2010, A&A, 521, L41+

Jørgensen, J. K., van Dishoeck, E. F., Visser, R., et al. 2009, A&A, 507, 861

Kristensen, L. E., Visser, R., van Dishoeck, E. F., et al. 2010, A&A, 521, L30+

Lada, C. J. 1999, in NATO ASIC Proc. 540: The Origin of Stars and Planetary Systems, ed. C. J. Lada & N. D. Kylafis, 143–+

Molinari, S., Brand, J., Cesaroni, R., & Palla, F. 1996, A&A, 308, 573

Ott, S., Science Centre, H., & Space Agency, E. 2010, ArXiv e-prints

Pilbratt, G. L., Riedinger, J. R., Passvogel, T., et al. 2010, A&A, 518, L1+

Poglitsch, A., Waelkens, C., Geis, N., et al. 2010, A&A, 518, L2+

van der Tak, F. F. S., van Dishoeck, E. F., Evans, II, N. J., & Blake, G. A. 2000, ApJ, 537, 283

Yıldız, U. A., van Dishoeck, E. F., Kristensen, L. E., et al. 2010, A&A, 521, L40+